UNIVERSITEIT VAN PRETORIA
UNIVERSITY OF PRETORIA
YUNIBESITHI YA PRETORIA

UNIVERSITEIT VAN PRETORIA
UNIVERSITY OF PRETORIA
YUNIBESITHI YA PRETORIA

Theoretical and Experimental Investigation of the Heat Transfer and Pressure Drop Optimisation on Textured Heat Transfer Surfaces

by

Marco Alfama (28157347)

Submitted in partial fulfilment of the requirements for the degree

MASTER OF ENGINEERING

in the Department of Mechanical and Aeronautical Engineering

University of Pretoria

February 2017

Supervisors: Prof J.F.M. Slabber and Prof J.P. Meyer

Abstract

Title: Theoretical and Experimental Investigation of the Heat Transfer and Pressure Drop Optimisation on Textured Heat Transfer Surfaces

Supervisors: Prof J.F.M. Slabber and Prof J.P. Meyer

Department: Mechanical and Aeronautical Engineering

Degree: Master of Engineering (Mechanical Engineering)

Modern nuclear reactors still use Zirconium-4 Alloy (Zircaloy®) as the cladding material for fuel elements. A substantial amount of research has been done to investigate the boiling heat transfer behind the cooling mechanism of the reactor. Boiling heat transfer is notoriously difficult to quantify in an acceptable manner and many empirical correlations have been derived in order to achieve some semblance of a mathematical model. It is well known that the surface conditions on the heat transfer surface plays a role in the formulation of the heat transfer coefficient but on the other hand it also has an effect on the pressure drop alongside the surface. It is therefore necessary to see whether there might be an optimum surface roughness that maximises heat transfer and still provides acceptably low pressure drop.

The purpose of this study was to experimentally measure pressure drop and heat transfer associated with vertical heated tubes surrounded by flowing water in order to produce flow boiling heat transfer. The boiling heat transfer data was used to ascertain what surface roughness range would be best for everyday functioning of nuclear reactors.

An experimental set-up was designed and built, which included a removable panel that could be used to secure a variety of rods with different surface roughnesses. The pressure drop, surface temperature, flow rate and heat input measurements were taken and captured in order to analyse the heat transfer and friction factors.

Four rods were manufactured with different roughnesses along with a fifth rod, which remained standard. These rods were tested in the flow loop with water in the upward flow direction. Three different system mass flow rates were used: 0kg/s, 3.2kg/s and 6.4kg/s. Six repetitions were done on each rod for the tests; the first repetition was not used in the results since it served the

purpose to deaerate the water in the flow loop. The full range of the power input was used for each repetition in the tests.

For the heat transfer coefficient at a system mass flow rate of 3.2kg/s, satisfactory comparisons were made between the test results and those found in literature with an average deviation of 14.53%. At 6.4kg/s system mass flow rate the comparisons deviated on average 55.45%. The velocity of the fluid in the test section was calculated from the pressure drop and was validated using separate tests. The plain rod, with no added roughness, was found to be the optimal surface roughness which is what is used in industry today.

The flow loop was in need of a couple of redesigns in order to produce more accurate results. Future work suggestions include adding more rods in the test section in order to investigate the nature of heat transfer in a rod bundle array as well as implementing all the suggested changes listed in the conclusion.

Keywords: heat transfer, roughness, boiling, nucleate boiling, flow boiling

Publications

Journal Article:

1. Theoretical and Experimental Investigation of the Heat Transfer and Pressure Drop Optimisation on Textured Heat Transfer Surfaces

Acknowledgements

Table of Contents

List of figures

List of tables

Nomenclature

General

Symbol	Description	Unit
V	Velocity or volts	$\frac{m}{s}$ or V
L/l	Length	m
g	Gravity	$\frac{m}{s^2}$
$z \text{ or } H$	Height	m
f	Friction factor	-
$D \text{ or } d$	Diameter	m
A	Area	m^2
p	Perimeter	m
Q	Heat transfer or volume flow rate	W or $\frac{m^3}{s}$
k	Thermal conductivity	$\frac{W}{m.K}$
K	Losses	-
T	Temperature	°C
r	Radius	m
h	Heat transfer coefficient or head	$\frac{W}{m^2.K}$ or m
C_p	Heat capacity	$\frac{J}{kg.K}$
Δ	Difference	-
q	Heat flux	$\frac{W}{m^2}$
h_{fg}	Enthalpy of vaporisation	$\frac{J}{kg}$
R	Roughness	m
Sa	Seebeck coefficient	-
P	Pressure or pitch	Pa or m
n	Prandtl constant	-
C/c	Constant	-
b/B	Bias error	%
p	Precision error or perimeter	% or m
R	Result error	%
m	Regression line gradient or Reynolds constant	-
t	Student multiplier	-
N	Data points	-
M	Measuring points	-
S	Standard deviation	-
S_{yx}	Best-fit error	-
S_{xx}	Summation of squares of x	-
x	x variable or thickness or single error	-or m or %
y	y variable	-

Symbol	Description	Unit
S_{xy}	Summation of squares of x and y	-
b	Bias best-fit gradient	-
a	Best fit	-
v	Degrees of freedom or kinematic viscosity	- or $\frac{m^2}{s}$
j	Colburn J-Factor	-

Greek Letters

Symbol	Description	Unit
ρ	Density	$\frac{kg}{m^3}$
μ	Dynamic viscosity	$\frac{kg}{m.s}$
α	Flow constant	-
ε	Roughness height	m
δ	Uncertainty error or boundary layer thickness	% or m
σ	Surface tension	$\frac{N}{m}$
v	Kinematic viscosity	$\frac{m^2}{s}$
θ	Contact angle	°

Subscripts

Symbol	Description
h	Hydraulic or hydrodynamic
e	Equivalent
c	Cross-sectional
o	Outer
i	Inner
1	Initial
2	End
∞	Arbitrary
v	Vapour
l	Liquid
cr	Critical
sat	Saturation
f	Fluid/Friction
s	Surface
c	Calculated
d	Diameter
a, b, c	Counters
M/m	End of series
i	Variable
t	Thermal
$flow$	Water flowing
$embedded$	Internally embedded

a	Average
q	Root mean square

Dimensionless Parameters

Symbol	Description
Re	Reynolds number
Pr	Prandtl number
Nu	Nusselt number

1 Introduction

1.1 Background

A nuclear power reactor has many components and all of them are designed with safety in mind. This goes hand in hand with efficiency to make it a viable method of energy production. The cladding is the outer tube where the fuel material is encased. This is a critical component of a reactor's performance as well as safety. The dissertation focuses on the heat transfer performance of the cladding where the heat produced in the fission process is transferred to the surrounding cooling water. This investigation requires knowledge of nuclear reactors and boiling heat transfer. A practical foundation in these branches of study will ensure a pragmatic and logical approach to optimising the cladding characteristics in terms of its thermo-hydraulic performance.

To explain the inner workings of a nuclear reactor, a general thermal reactor design is used. The core consists of the cladding-encased fuel material, the coolant and the moderator [1]. The cladding is used to contain the fission products from entering and contaminating the coolant. For a light-water reactor (LWR), the coolant also acts as the moderator. The function of the moderator is to reduce fast energy neutrons to slower energy neutrons. The interface between the coolant and the cladding dictates how heat is transferred and carried away. Cladding material is essential for the safety of any modern-day reactor. The cladding layer should have low neutron absorption, be structurally sound, not react with the coolant and transfer heat efficiently. This purpose of the material is critical in a reactor's operation as the cooling is designed to be as effective as possible.

Boiling occurs along a generally accepted trend line with different regimes. These regimes can be divided into three sections; firstly, convection heat transfer where no bubbles are seen; secondly, nucleate boiling where an increase in heat transfer as bubble nucleation sites provide starting points for bubble creation and growth providing a stirring action; thirdly, film boiling occurs when water vapour covers the heating element and retards the ability for heat to escape, thereby decreasing heat transfer abilities. Film boiling is the regime that is transitioned into once the critical heat flux (CHF) is reached and is more commonly known as "burnout". Zircaloy® has been widely used in LWRs in the past. Initially, stainless steel was used but due to the improved neutron interaction and corrosion resistance, Zircaloy® replaced stainless steel [2].

1.2 Objectives

The purpose of the study was to experimentally measure pressure drop and heat transfer associated with vertical heated tubes surrounded by upward flowing water in order to produce flow boiling heat transfer. The tests were predominantly in the turbulent flow regime. The main objective was to study the effect of surface roughness on the heat transfer from the surface of a heated tube emulating a part of a fuel pin in a reactor. It was expected that the increase in surface roughness would increase the turbulence of the coolant alongside the tube resulting in an increase in the heat transfer coefficient. Increasing the heat transfer capability would lead to cooler fuel. On the other hand, a rougher surface would increase the pressure drop resulting in an increase in the required pumping power, having a negative impact on the running costs of the plant. Therefore, the objective of the study was to evaluate the relation between heat transfer and pressure drop and whether the roughness could be optimised to serve both the fuel temperature and pressure drop minimisation.

The tests were done in a flow loop designed to do a number of thermo-hydraulic tests on heated surfaces [3]. In this loop a number of specifically configured test set-ups can be accommodated depending on the nature of the research to be done. The tests are then fixed to a removable panel which locates the test specimen in the testing chamber of the loop.

An experimental set-up was designed and built, which included a special attachment to secure a variety of rods with different surface roughnesses onto the removable panel. The pressure drop, surface temperature, flow rate and heat input measurements were to be taken and captured in order to analyse the heat transfer and friction characteristics. Five rods were to be tested in the flow loop in order to achieve a preferred roughness range. The boiling heat transfer data would be used to ascertain what surface roughness range would best improve the everyday economic functioning of nuclear reactors.

1.3 Overview of the dissertation

The five chapters following the introduction contain the procedure followed in order to arrive at a logically deduced conclusion. The literature study in Chapter 2 covers a number of relevant studies applicable to this field. The experimental set-up in Chapter 3 details the flow loop used for all the experiments including the procedure followed to attain the relevant results. The results in Chapter 4 succinctly detail all the applicable experimental data, while the analysis of results in Chapter 5 offers a logical interpretation of the results. The last chapter summarises the experiments and arrives at an all-encompassing conclusion for the objectives detailed above.

2

2 Literature study

2.1 Introduction

Boiling is a phenomenon crucial to a nuclear reactor. Boiling has been studied extensively but there are specific sections in the field which remain weak from a theoretical aspect. There is presently no widely accepted and accurate mathematical model of the nucleate boiling phenomenon due to its complex nature. The sometimes unpredictable nature of boiling makes it tough to develop trustworthy theoretical models, and therefore, empirical models are used.

2.2 Fundamentals of fluid flow and heat transfer

To understand the mechanics of surface roughness optimisation, some general concepts are vital to the investigation of the heat transfer involved. The next section defines and lays out the basic parameters used in developing a test schedule.

2.2.1 Reynolds number

The Reynolds number is a dimensionless parameter discovered by Osborn Reynolds in the 1880s and is the ratio of inertia forces to viscous forces [4]:

$$Re = \frac{\rho V L}{\mu} \tag{1}$$

The denominator in this equation represents the viscous forces attempting to keep the flow smooth but if the fluid density and velocity are high, the viscous forces are overcome and turbulent flows prevail.

2.2.2 Friction analysis

A control volume model is used to describe the fluid flow in a pipe. There are different contributing factors, which are easily articulated in the incompressible steady flow energy equation such as the potential and kinetic energy of the fluid [5]:

$$\left(\frac{P}{\rho g} + \alpha \frac{V^2}{2g} + z \right)_1 = \left(\frac{P}{\rho g} + \alpha \frac{V^2}{2g} + z \right)_2 + h_{turbine} - h_{pump} + h_{friction} \tag{2}$$

If the pipe has constant diameter:

$$\Delta h_{tot} = h_f + \Sigma h_m = \frac{V^2}{2g} \left(\frac{fL}{d} + \Sigma K \right) \tag{3}$$

Julius Weisbach, in 1850, published the following correlation, which incorporates the approximation of h_f being proportional to V^2 [5]:

3

$$h_f = f \frac{L}{D_e} \frac{V^2}{2g} \tag{4}$$

The equation neglects minor losses and can be used as the pump head [5]:

$$h_{pump} = \frac{Power}{\rho g Q} = h_f = f \frac{L}{D_e} \frac{V^2}{2g} \tag{5}$$

The factor f is called the Darcy friction factor and is a dimensionless parameter used to correlate the relative roughness, $\frac{\varepsilon}{d}$, to the Reynolds number [5]. The relative roughness is the ratio of the average roughness height to the equivalent diameter of the pipe [4]. To automate the friction factor, an approximate equation, proposed by Haaland in 1983, can be used. The equation does not require any iteration [5]:

$$\frac{1}{f^{\frac{1}{2}}} \approx -1.8 \log \left[\frac{6.9}{Re_d} + \left(\frac{\frac{\varepsilon}{D_e}}{3.7} \right)^{1.11} \right] \tag{6}$$

Equations 2 to 5 can be used to relate the pressure drop to the appropriate physical effect. Pressure drop is defined as the difference in pressure experienced between two points due to varying factors impeding the flow of the fluid. A pressure drop can be produced by introducing surface effects, height differences and temperature differences. This is because each of these affects some of the parameters in the general pressure equation [5]:

$$P = \rho g h$$

Height differences change the gravity and height factors and temperature differences affect fluid densities. Surface effects change the physical characteristics the fluid must overcome to pass through. **Equation 2** is simply an expression of the conservation of energy. Therefore, pressure drop is the difference in pressure between two points:

$$\Delta P = P_1 - P_2$$

2.2.3 Flow in tubes

Flow can be categorised into three different and distinct flow regimes. The first is called laminar flow and is identified by its smooth-flowing characteristic at relatively low velocities. The second is called transitional flow and occurs when the flow starts to change its flowing nature and is not so smooth anymore with some agitation. This happens when the flow becomes turbulent, which

is the third flow regime. Turbulent flow is highly agitated and looks chaotic with very little or no order [4]. Flow in a tube becomes turbulent in most cases with a Reynolds number above 4 000 [4].

Hydraulic diameter is used to characterise the cross-section and, in circular tubes, is defined by the diameter [4]. The general relation that can be used for any geometry is [4]:

$$D_h = \frac{4A_c}{p} = D \tag{7}$$

and flow through an annulus:

$$D_h = D_o - D_i \tag{8}$$

The velocity boundary layer is defined as the cross-sectional profile of how the surface friction affects the velocity. At the surface boundary, the friction forces are strong and effectively slow down the flow compared with the centre area where the friction effect is less and flow moves through the tubes with more ease. The hydrodynamic entrance region is the length, L_h, where the velocity profile fully develops and remains constant throughout the rest of the tube. This length is important to note as taking measurements in the middle of the hydrodynamic entrance region does not yield accurate results of what is really happening in the tube. Once the flow is fully developed, the velocity profile will settle and become straighter [4].

A similar mechanism of development occurs with the fluid temperature and is called the thermal entrance region. This is the length where the thermal boundary layer, L_t, develops. When the thermal profile settles due to the surface temperature, the thermal boundary layer is fully developed. At turbulent Reynolds numbers, the effect of the Reynolds number becomes less and an approximation of both the velocity and thermal entrance lengths can be calculated [4]:

$$L_{h,turbulent} \approx L_{t,turbulent} = 10D \tag{9}$$

2.2.4 Heat transfer

Fourier's law of heat conduction is used to characterise the heat transfer through a wall with known thermal conductivity:

$$Q_{cond,wall} = -kA\frac{dT}{dx} = kA\frac{(T_1 - T_2)}{L} \tag{10}$$

5

As can be noted, the thickness of the wall, L, is inversely proportional to the heat conduction through the wall. This piece of information is used when considering the thickness of the cladding. The cylindrical shape of the rod is assumed to be simplified into a block with linear heat transfer. This was done due to the thin wall of the rod as well as the high thermal conductivity of the rod. Heat transfer is in one direction.

Newton's law of cooling is used to express convection heat transfer on the surface and depends on many fluid properties along the fluid velocity [4]:

$$Q = hA_s(T_s - T_\infty)$$

(11)

The convection heat transfer coefficient, h, between a surface and a fluid can be calculated with the above relation with end result units of $\frac{W}{m^2.K}$ [4].

It has been shown that for most gases, organic liquids, ordinary and heavy water, flowing in a long straight channel with high Reynolds numbers in the turbulent regime, the heat transfer coefficient relation is expressed as [1]:

$$h = C\left(\frac{k}{D_e}\right)Re^m Pr^n$$

(12)

The fluid properties are most often taken at the bulk fluid temperature. The Dittus-Boelter equation uses the constants $C = 0.023$, $m = 0.8$ and $n = 0.4$. These constants are used for circular tubes and can be used for other geometries by adjusting the equivalent diameter [1]. This method can yield high inaccuracies. Appropriate variables can be calculated for ordinary water flowing parallel to the axis of a lattice of rods in a square configuration [1]:

$$C = 0.042\frac{P}{D} - 0.024$$

(13)

where $1.1 \leq \frac{P}{D} \leq 1.3$ and $m = 0.8$ with $n = 0.333$

There are a variety of heat transfer coefficient and Nusselt number correlations for internal forced convection situations. The main area of focus in nuclear applications is flow in the turbulent regime. A commonly used relation for turbulent flow in a tube is the Dittus-Boelter relation, developed in 1930, which is applicable to fully developed flow in smooth tubes. It does not consider the surface roughness [4]:

$$Nu = 0.023Re^{0.8}Pr^n$$

(14)

6

The limitations of this equation are $0.7 \le Pr \le 160$ and $Re > 10000$ where $n = 0.4$ for heating and $n = 0.3$ for cooling [4].

Sieder and Tate, in 1936, developed a relation that can be used when the temperature difference between the surface and the bulk fluid is large [4]:

$$Nu = 0.027 Re^{0.8} Pr^{\frac{1}{3}} \left(\frac{\mu}{\mu_s}\right)^{0.14} \tag{15}$$

The limitations of this equation are $0.7 \le Pr \le 17600$ and $Re \ge 10000$.

The second Petukhov equation, developed in 1970 [6], improves accuracy by up to 15% compared with the Dittus-Boelter and Sieder and Tate relations [4]:

$$Nu = \frac{\left(\frac{f}{8}\right) Re Pr}{1.07 + 12.7 \left(\frac{f}{8}\right)^{0.5} \left(Pr^{\frac{2}{3}} - 1\right)} \tag{16}$$

The limitations of this equation are $0.5 \le Pr \le 2000$ and $10000 < Re < 5x10^6$.

The accuracy of this equation can be further improved at low Reynolds numbers as Gnielinski did in 1976 [4]:

$$Nu = \frac{\left(\frac{f}{8}\right) (Re - 1000) Pr}{1 + 12.7 \left(\frac{f}{8}\right)^{0.5} \left(Pr^{\frac{2}{3}} - 1\right)} \tag{17}$$

The limitations of this equation are $0.5 \le Pr \le 2000$ and $3000 < Re < 5x10^6$.

As can be noted, the second Petukhov and Gnielinski relations take into account the friction factor. The Gnielinski equation is the preferred choice from the above [4].

Monrad and Pelton, in 1942, proposed a relation for an annulus specific geometry, which can be compared with the above [7]:

$$Nu = 0.02 Re^{0.8} Pr^{\frac{1}{3}} \left(\frac{D_2}{D_1}\right)^{0.53} \tag{18}$$

The limitations of this equation are $0.7 < Pr < 120$, $Re > 10000$ and $\frac{L}{D} > 60$.

7

Typical values of the heat transfer coefficient were looked up in order to compare resultant values. For forced convection with water flowing in pipes, expected heat transfer coefficients are in the range of $250 - 12000 \frac{W}{m^2.{}^\circ C}$ [7]. When dealing with boiling water flowing in a tube, the expected range is $5000 - 100000 \frac{W}{m^2.{}^\circ C}$ [7].

The PATRICIA test section was a set of tests done to simulate exactly what happens in a nuclear reactor under the same working conditions and parameters [8]. This study focused on modelling the clad-to-coolant heat transfer in the midst of a reactivity-initiated accident (RIA). An Inconel tube was used instead of Zircaloy® because of the difficulties welding the thermocouples to the inner surface. Pool boiling along with flow boiling was tested in the study (15 MPa, 280 ℃, 4m/s). The rod was 600mm long, with an inner diameter of 8.8mm, outer diameter of 9.5mm and hydraulic diameter of 14.2mm [8]. The experiments showed that the clad heating rate largely affected the clad-to-coolant rate. This has a profound effect on the boiling curve shifting according to the clad heating rate. This is another factor that must be considered when analysing any boiling curve [8].

2.2.5   Boundary layers in turbulent flow

Boundary layer flow characteristics vary depending on a number of factors including surface roughness, fluid properties, geometry and temperature. With parallel flow, the critical distance (x_{cr}) is defined as the distance of the laminar flow regime before the flow is transitioned to turbulent flow. This measure of flow is done with a dimensionless parameter named the critical Reynolds number [4]:

$$Re_{cr} = \frac{\rho V x_{cr}}{\mu} = 5 \times 10^6$$

(19)

Two types of boundary layers are commonly referred to. They are the velocity and thermal boundary layers. These two are related since the one greatly affects the other [4].

The velocity boundary layer considers the velocity variation of flow over an object with the perpendicular distance away from the object acting as the variable. The velocity variation is due to a no-slip condition and characterises the particles of the flow right next to the object as effectively not moving. If one considers the varying flow velocities as layers on top of one another, this non-moving layer influences the adjacent layer acting like a viscous force slowing down the particles [4].
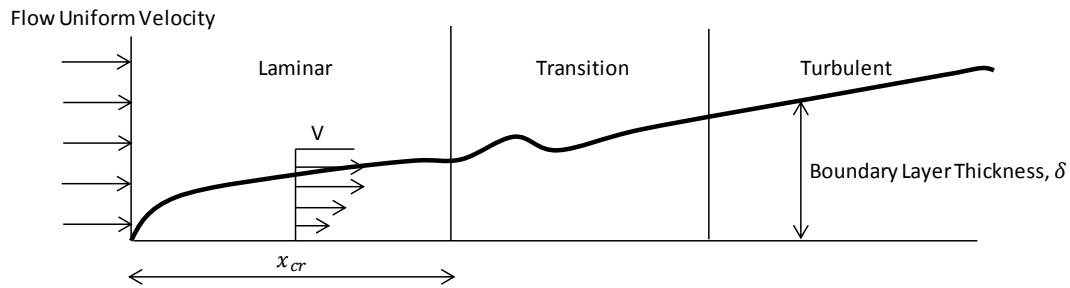
Figure 1 Velocity boundary layer over a flat plate [4]

In **Figure 1**, δ is the velocity boundary layer thickness and is the perpendicular distance away from the plate where a no-slip condition still affects the velocity of the flow. The line distinction is theoretically made to be where the flow is at 99% of the free-stream velocity. Inside the boundary layer line, the viscous effects are still present, whereas outside the line, viscous effects are virtually zero [4].

The velocity boundary layer thickness of a laminar flow fluid over a flat plate (isothermal) is [4]:

$$\delta = \frac{4.91}{\sqrt{\frac{V}{vx}}} \tag{20}$$

The velocity boundary layer thickness of a turbulent flow fluid over a flat plate (isothermal) is [4]:

$$\delta = \frac{0.38x}{(Re_x)^{\frac{1}{5}}} \tag{21}$$

Within the boundary layer, there are three further layer definitions. The viscous sublayer is where the viscous effects are dominant, while in the buffer layer, the turbulence is becoming a stronger driving factor and in the turbulent layer, the turbulence is dominant [4].

The thermal boundary layer develops due to the difference in temperature when a fluid moves over a surface. If one considers the varying temperatures as layers on top of one another, the bottom layer in contact with the surface will steadily reach thermal equilibrium. Similar to the velocity boundary layer, a profile develops and in this case, it is a temperature profile. This temperature profile transitions from the surface temperature to the mixed mean fluid temperature. The layers transfer energy with each other creating the profile [4].
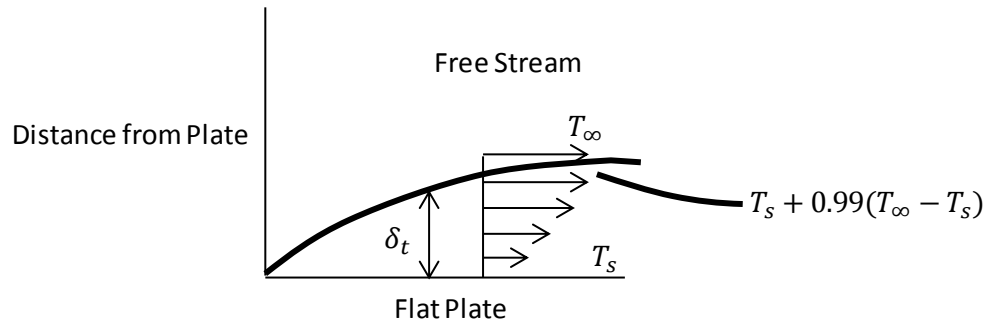
Figure 2 Thermal boundary layer over a flat plate [4]

The term, δ_t, is the thermal boundary layer thickness and is depicted in **Figure 2**. This thickness is governed by the temperature difference between the measured temperature in the fluid and the surface temperature equating to 99% of the temperature difference of the fluid and surface temperature. The temperature gradient is directly related to the rate of convection heat transfer, therefore, the shape of the thermal boundary layer is significant [4].

The thermal boundary layer thickness of a laminar flow fluid over a flat plate (isothermal) is [4]:

$$\delta_t = \frac{\delta}{Pr^{\left(\frac{1}{3}\right)}} = \frac{4.91x}{Pr^{\left(\frac{1}{3}\right)}\sqrt{Re\_x}} \tag{22}$$

A specific dimensionless number was introduced by Ludwig Prandtl to relate the velocity and thermal boundary layers and can be applied to tubes [4]:

$$Pr = \frac{\mu C_p}{k} \tag{23}$$

The basic theory found in **Section 2.2.5** can be applied to tubes.

2.3 Fundamentals of boiling heat transfer

2.3.1 Background

Boiling is a phenomenon found in many real-life applications and occurs when a surface heats up a liquid in contact with it and that is flowing or is stagnant and when the temperature of the surface is somewhat greater than the saturation temperature of the liquid. When boiling starts, bubbles form and rise due to the effect of buoyancy. Surface tension is what makes it possible for bubbles to form because the boiling interrupts the equilibrium forces in the liquid. There are two types of boiling: pool boiling and flow boiling. Pool boiling constitutes boiling taking place

10

while the fluid in the interaction is not moving or relatively stagnant and flow boiling is with the fluid moving [4].

2.3.2 Pool boiling

Natural Convection   Nucleate   C   Transition   Film

$\dot{q}_{Boiling} \left(\dfrac{W}{m^2}\right)$

10^6

10^5

10^4

10^3

~ 5 10 ~ 30 100 ~ 120 1000

$\Delta T_{excess} = T_s - T_{sat}$ (°C)
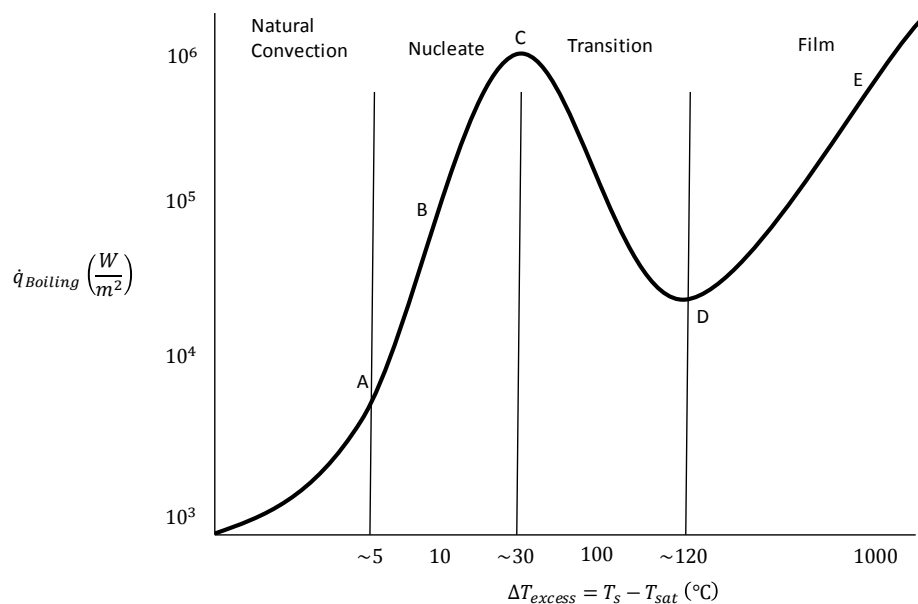
Figure 3 Boiling curve for water at 1atm [4]

In **Figure 3**, the boiling curve can be observed. This research was done by Nukiyama in 1934 and paved the way in how researchers classify boiling [9]. The tests explained how each regime was brought about.

In **Figure 3,** the *x-axis* is the temperature difference between the saturation temperature at that pressure and the heated temperature of the surface. The *y-axis* is the heat transfer rate per unit area (W/m^2). In the beginning, when natural convection starts, bubbles are not seen forming but as the temperature difference increases, bubbles will most likely start forming at this stage but will collapse quickly. At the initial nucleate boiling stage, bubbles will form and detach themselves from the surface as they rise up and dissipate there. The area left vacant by the rising bubble will form another bubble with the new liquid in contact with it [4].

The Rohsenow equation, proposed in 1952, is still widely used as an approximation of the heat transfer during nucleate boiling. This equation has an expected error of $\pm$ 100% when calculating the heat flux for a known temperature difference and can be used for smooth and relatively smooth surfaces. The error drops to 30% when calculating the temperature difference

11

for a known heat flux [4]. This is due to the erratic nature of bubbles as their formation really starts to gain momentum [4]:

$$\dot{q}_{nucleate} = \mu_l h_{fg} \left[\frac{g(\rho_l - \rho_v)}{\sigma} \right]^{\frac{1}{2}} \left[\left(\frac{c_{pl}(T_s - T_{sat})}{C_{sf} h_{fg}} \right) \Pr l^{-n} \right]^3 \qquad (24)$$

This process is continuous and promotes good heat transfer. The later stage of nucleate boiling sees the bubbles popping at the surface. The reason the incremental increase per degree of temperature difference reduces is because a blanket of bubbles partially covers the surface providing the heat; therefore, making it difficult to transfer the heat to the liquid which it is not directly in contact with. The highest point in **Figure 3** is called the critical heat flux (CHF) [4]:

$$\dot{q}_{max} = C_{cr} h_{fg} [\sigma g \rho_v^2 (\rho_l - \rho_v)]^{\frac{1}{4}} \qquad (25)$$

Passing this point proves hard to predict the boiling characteristics. In film boiling, a period of transition occurs where nucleate boiling and film boiling happen before becoming fully film boiling. During this transition, the blanket of bubbles completely covers the surface, thereby decreasing the rate of heat transfer. It comes to a point where radiation through the film of coalesced bubbles heats up the liquid. Two important points to understand are the departure from nucleate boiling (DNB) and the minimum film boiling (MFB) points. The DNB is another term for CHF and the MFB is where transitional film boiling becomes fully film boiling commonly known as the Liedenfrost point [10]:

$$\dot{q}_{film} = C_{film} \left[\frac{g k_v^3 \rho_v (\rho_l - \rho_v) \left[h_{fg} + 0.4 c_{pv}(T_s - T_{sat}) \right]}{\mu_v D(T_s - T_{sat})} \right]^{\frac{1}{4}} (T_s - T_{sat}) \qquad (26)$$

When the surface is temperature controlled, the process will follow the curve as outlined in the previous paragraph. If it is controlled by the rate of heat transfer, then the temperature will spike after the DNB, taking it straight into the film boiling region. This phenomenon can be very dangerous in reality when temperature control and a high heat transfer are vital to an operation [10]. This point is critical in nuclear engineering because it can lead to overheating of the fuel and degradation of the clad leading to the release of radioactivity. In industry, this point will be avoided at all costs, thereby limiting the surface temperatures.
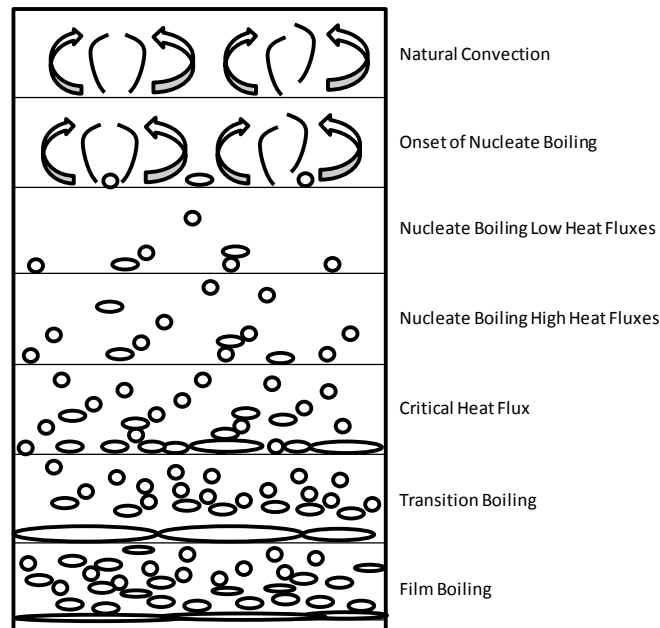
Figure 4 Bubble growth in pool boiling [10]

Figure 4 demonstrates the bubble formation throughout the different stages. These regimes were established by the work of Collier and Thome in 1994 [10].

2.3.3 Flow boiling

Flow boiling encompasses the similar boiling nature found in pool boiling with the exception of the fluid in contact with the heating surface being forced to flow past. This drastically changes the heat transfer capabilities [11].

There are two main classifications of flow boiling, namely sub-cooled boiling and saturated boiling. Sub-cooled boiling refers to the boiling taking place between the fluid and the heating surface only. Saturated boiling occurs when all the fluid in contact with the heating surface is at the saturation temperature of those conditions [11]. There are four heat transfer mechanisms when nucleate boiling takes place in flow boiling [12]:

- evaporation heat transfer through the bubble from the heated surface (onset of nucleate boiling);
- single-phase convection heat transfer through the wetted surface (onset of nucleate boiling);
- latent heat transfer when the bubble detaches (fully developed nucleate boiling);
- liquid-vapour heat transfer as the bubble detaches from the surface (fully developed nucleate boiling).

13

The first two mechanisms are predominant in early partial nucleate boiling, while the last two mechanisms dictate heat transfer when it becomes fully developed [12].

2.3.4 Bubble dynamics

Surface conditions play a major role in boiling performance. Bubbles form from an existing vapour deposit between the heating surface and the fluid. Therefore, the parameters of the physical surroundings of the vapour deposit are important in determining any working characteristics of the process at hand. The vapour deposits can be found in any small drastic surface changes such as varying surface roughnesses. The crevices with vapour deposits are called cavities and supply crucial data to how the heat transfer will perform [11]. This work was investigated by Bankoff in 1958 and still remains relevant.
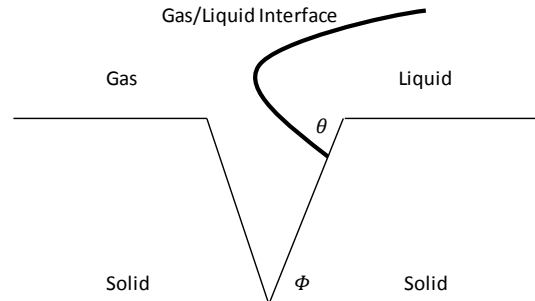
Figure 5 Gas entrapment process [11]

The contact angle is defined as θ, as can be seen in **Figure 5**. The condition that must be met for the gas to be trapped is [11]:

$$\theta > 180° - 2\Phi \tag{27}$$

Bubbles grow because latent heat is transferred to the bubbles, which originate in cavities [11]. There is a distinct difference in bubble behaviour when comparing pool boiling and flow boiling. The surface tension forces are holding the bubble on the heated surface. The forces around the bubble affect the shape of the bubble, therefore, in pool boiling where everything is balanced, a spherical shape is achieved, while in flow boiling, the forces are not balanced and the shape is irregular. Contact angles in pool boiling are generally consistent and in flow boiling, they vary significantly. The contact angles of the front and back of the bubble with respect to the direction of flow will be different [13].

2.3.5 Factors influencing boiling

Many factors influence the phenomena of boiling such as the atmospheric conditions and the surfaces involved in the heat transfer, but a factor often neglected which requires further investigation is the effect of dissolved gases found in the boiling medium, in this case, it is water. Kandlikar and Steinke, 2002, investigated the effect of dissolved gases on heat transfer and drew many applicable conclusions [14]. Three air concentrations were analysed at 1.8, 5.4 and 8 ppm where 8.6 ppm was the reported average of tap water. Nucleation was initiated at 90.5 ℃ for the 8 ppm gas concentration, while the others reached almost 100 ℃ before nucleation was noted [14]. This demonstrably communicates the effect of dissolved gas in the water being used for the tests and can significantly distort readings when they are not placed in context.

2.4 Fundamentals of surface roughness

2.4.1 Background

Surface roughness is simply defined as the surface profile. If the profile has high peaks which are closely spaced, the surface is generally referred to as rough. There are some other common parameters used to characterise the surface: waviness and lay. Waviness describes the motion of the profile, which is more widely spaced, and lay describes the main direction of the roughness pattern. Certain inconsistencies can occur on the surface such as small cracks or scratches but these do not form part of the general surface characterisation [15]. When detailing the surface, two key measurements make up the roughness. The one is the average height of the peaks, R_a, and the other is the distance from one peak to the other, D [15]. Both of these are illustrated in **Figure 6**. There are two different definitions of roughness. The first is the average roughness as mentioned before, R_a, and is commonly used in many industries. The second is the root mean square (RMS) roughness, R_q, and is commonly used for optical components [15].
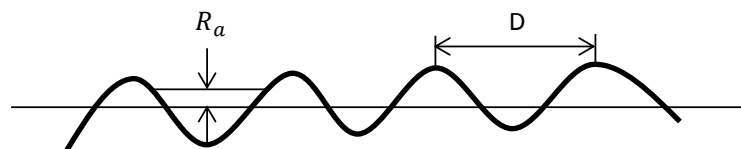
Figure 6 Common surface measurements [15]

Measuring surface roughness can be a tougher task than expected when an accurate measurement is needed. There are many present methods used to measure surface roughness and one of the most common is physically tracing the profile. A mechanical stylus moves in the intended direction and traces the surface for a specified distance. The degree of accuracy achieved using this method is often limited by the size of the stylus tip. The bigger the stylus tip, the harder it is for the stylus tip to accurately read the fine terrain [16].

Surface roughness parameters, such as the average roughness (R_a) and RMS roughness (R_q), have been reported to be inefficient in describing nucleate boiling data but many researchers have done successful work. There are inherent problems associated with these surface roughness parameters. The possible reason for any inaccuracies must be acknowledged in determining the validity of the results found in this dissertation. Optical or electron microscopy may be used to measure cavity shapes and sizes to provide a more accurate alternative [17]. Researchers use three methods to increase heat transfer in the same area [18]:

- Increase the number of bubbles.
- Shorten bubble surface existence period.
- Lower nucleate boiling temperature.

The focal point of the optimisation in this research was the surface roughness of the fuel pin. One of the most commonly practised methods of optimising heat transfer is changing the surface roughness. The theory about this process is that the surface roughness changes the number of nucleation sites on the heating surface and possibly contributes to shifting the boiling curve. The surface roughness can play a role in influencing the boiling curve. The increased roughness causes a stirring action, which is beneficial to heat transfer [18]. Turbulent flow consists of chaotic flow, which improves the rates of momentum and heat transfer within the fluid [4].

In 1936, Jakob noted how surface effects and the level of oxidation and corrosion affected the boiling curve [17]. The first experiments investigating surface roughness in the field of boiling and its effects were done by Corty and Foust but it was not until Rohsenow, in 1952, that surface effects were taken into account in the general boiling equations [18]. The idea of improving heat transfer by introducing roughness effects is that the temperature difference necessary for a certain heat flux drops, thereby increasing boiling heat transfer [18]. The importance of this study for vertical tubes is magnified when previous studies have noted higher

heat transfer rates in vertical tubes than in horizontal tubes under pool boiling conditions [18]. One study in particular reported a 230% increase in heat transfer in vertical tubes compared with horizontal tubes [18].

Creating a surface texture can be complicated when considering the accuracy of the method and the uniformity of the method. Machining can vary significantly if the same roughness needs to be achieved again in the future; therefore, sandblasting is used. Sandblasting incorporates blasting a specific material, also called grit, at the surface where the roughness is intended. The size and the material of the grit used to blast are very important and directly influence the outcome. The pressure used to blast can also impact the outcome.

2.4.2 Surface roughness measurement

Roughness measurements are crucial for experiments and therefore care must be taken with these measurements. Surface roughness is commonly measured by using a type of probe to move along the surface and record the oscillations. A second option is to use an atomic force microscope (AFM), which uses a flexible cantilever to map out the topography. A third option is a laser scanning system, which is a non-contact method [16]. These processes can map out a specific area and detail the landscape according to the many different definitions. The question remains: which method is the most accurate as well as the most appropriate for the present study? Factors that can hinder the comparison of the above measuring methods must be considered, as follows [16]:

- scan speed;
- surface probe size;
- reflectivity of material being measured;
- uniformity of roughness;
- number of tests done;
- data reduction techniques used to process the raw data;
- pronouncement of the surface features.

A common assumption related to surface roughness is that the size of the tip directly predicts the roughness outcome, but a study conducted by the Oak Ridge National Laboratory [16] refers to this as a possible misconception due to the stylus producing higher peak-to-valley roughness values than the AFM even though the AFM uses finer tips. The finer the tip, the deeper the tip can penetrate the valley and as a result produce a more accurate and larger

roughness result but this was not the case. The study lists equipment calibration error and the stylus tip bouncing as possible explanations [16]. Ultimately, the study concludes that one method is not superior to another but rather the choice needs to be made specific to the situation. For this research, a probe passed over the surface was used to record the oscillations.

2.5 Instrumentation

Thermocouples are common and inexpensive temperature measuring devices used in many engineering applications. The thermocouples are based on a principle discovered by Thomas Seebeck in 1821. The principle involves a voltage existing in a conductor which experiences two different temperatures on each opposite side. This voltage occurs due to the electrons moving around. When the hotter side of the conductor is heated, the electrons are energised and travel towards the colder end, see **Figure 7**. This movement creates an electrostatic voltage. If the ends were at the same temperature, no voltage would be measured. The difference in voltage is proportional to the temperature difference A thermocouple works on a relative basis, which makes its range in applications broad [19].
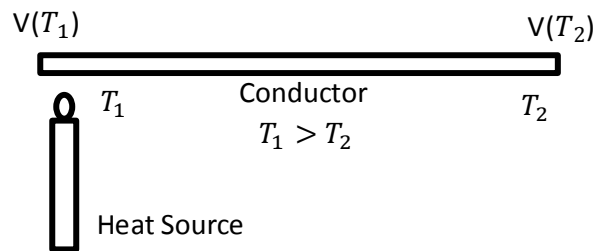
Figure 7 Basic thermocouple theory [19]

The voltage is calculated using the Seebeck coefficient (Sa) and contains all the material characteristics [19]:

$$V = Sa(T1-T2)$$

(28)

Thermocouples are made by joining two conductors together and applying them to the surface temperature in question. This junction is called the hot junction and the other end is the cold junction. The difference in temperature between the two conductors induces a voltage. This voltage is measured by a measuring device and is used to determine the temperature but it is vital that the cold junction temperature is known [20]. Cold junction compensation (CJC) is something to be carefully noted because the accuracy of the readings can be affected if not accounted for and understood. CJC is often done by the measuring device. The temperature of

18

the cold junction needs to be added to the hot junction reading in order to avoid reading the temperature difference of the junctions but to successfully read the absolute temperature of the surface in question [20].

Errors are unavoidable in measuring devices but there are ways of improving the degree of accuracy. Knowing where the error originates from can serve to expect the outcome and make provisions for it. There are three possible errors associated with thermocouples [21]:

- lead wires thermal energy conduction;
- radiation heat transfer from surrounding surfaces;
- transient temperature lag.

2.6 Summary

The previous work done reviewed in this chapter demonstrated the complexities of boiling heat transfer and the effect of the surface roughness on the heat transfer. A number of researches were discussed, communicating the possibilities of surface roughness on the heat transfer medium. Nukiyama proposed the first boiling curve, which is generally referred to today, while the work of Rohsenow assisted in creating a mathematical model, but until the present day, there is no standard on how to analyse boiling. This chapter also researched internal forced convection. This knowledge enables better understanding of the test results.

3 Experimental test rig

3.1 Introduction

All facets of the experimental set-up are detailed in this chapter and serve to explain how the tests were done. The validation of the test rig is outlined along with descriptions of the test sections. The experimental procedure as well as the data reduction is shown in order to better describe the nature of the results. An uncertainty analysis was done to take into account all possible inaccuracies that could play a role in affecting the final results and conclusion.

3.2 Experimental set-up

Two major sections of the test rig must be focused on, namely the flow loop and the removable panel where the test specimens are placed. The design and building of the test rig was the deliverable of another master's degree and was free to be used for the objectives of this research [3]. The author of this dissertation assisted in the design and building of the test rig. Partial designs and machining of the removable panel were done by the author along with other sections of the flow loop.

3.2.1 Flow loop

Figure 8 is a computer-aided design (CAD) depicting the full test rig. The entire flow loop was manufactured from stainless steel in order to prevent corrosion and leaching from the rig to the water. The stainless steel prevented many possible issues but with it came many challenges. The main challenge was the machining and welding of all the separate parts. Where mild steel was easier to work with, stainless steel required more experience and skill and was therefore outsourced to a skilled welder from the Sasol laboratories found on the University of Pretoria's campus. The welding was completed in such a way that leaks would not be prevalent and thus maintain the integrity of the flow loop, which is paramount when working with pressure.

The water quality was of the utmost importance as impurities could affect the final results and with so many tests being run, it would be easy to contaminate the water over time. A Y-strain filter was installed under the repressuriser in order to separate unwanted finite debris. Distilled water was used in order to maintain quality control and this was sourced from the Civil Engineering laboratories at the University of Pretoria. A pressurised tank filled with this water was placed outside the test rig room and was used to supply the water as well as pressurise the system. Careful control of this area enabled good and stable control of the flow loop pressure.
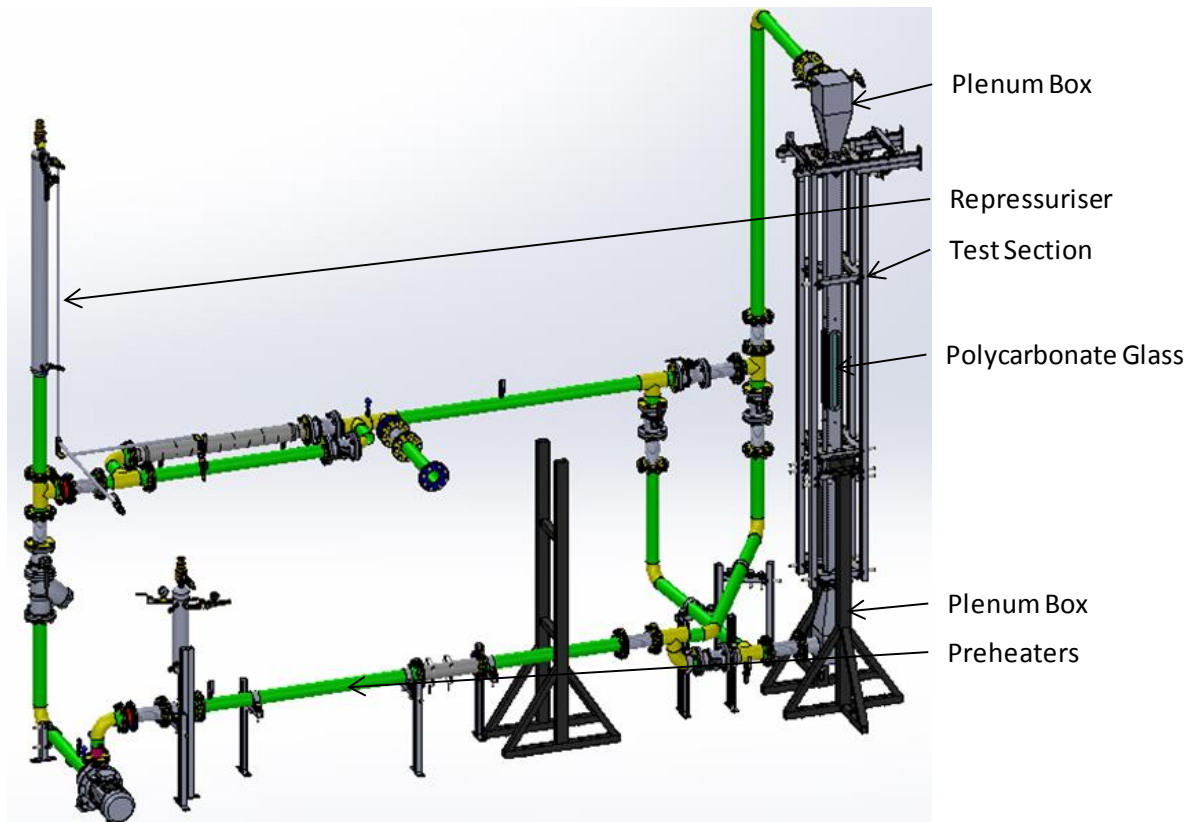
Figure 8 CAD model of the flow loop [3]

A venturi flow meter was used to measure the flow rate. This was done in conjunction with a differential pressure transducer, which was connected to the venturi by impulse lines. An average pressure was measured by the differential pressure transducer. The company Endress+Hauser kindly donated the differential pressure transducer, which was tested and calibrated at their laboratory [22].

A centrifugal pump connected to a variable speed drive (VSD) was used to pump the water through the system. Three system mass flow rates were used in the tests: 0kg/s, 3.2kg/s and 6.4kg/s were the flow rates explored. This range covered pool boiling as well as two other flow boiling scenarios. Going any higher resulted in unacceptable cavitation in the pump. Plenum boxes were used above and below the test section and assisted in providing flow uniformity for the fluid entering and exiting the test section. A flow straightening honeycomb was used at the test section outlet to assist with flow uniformity. Preheaters were used to help preheat the coolant in the bulk fluid because all tests were conducted at a specific initial temperature. In order to retain the heat build-up in the flow loop, 20mm thick Armaflex insulation was placed all

21

over the flow loop covering most of the stainless steel pressure boundary. A partial piping and instrumentation diagram (PID) can be seen in **Figure 9**.
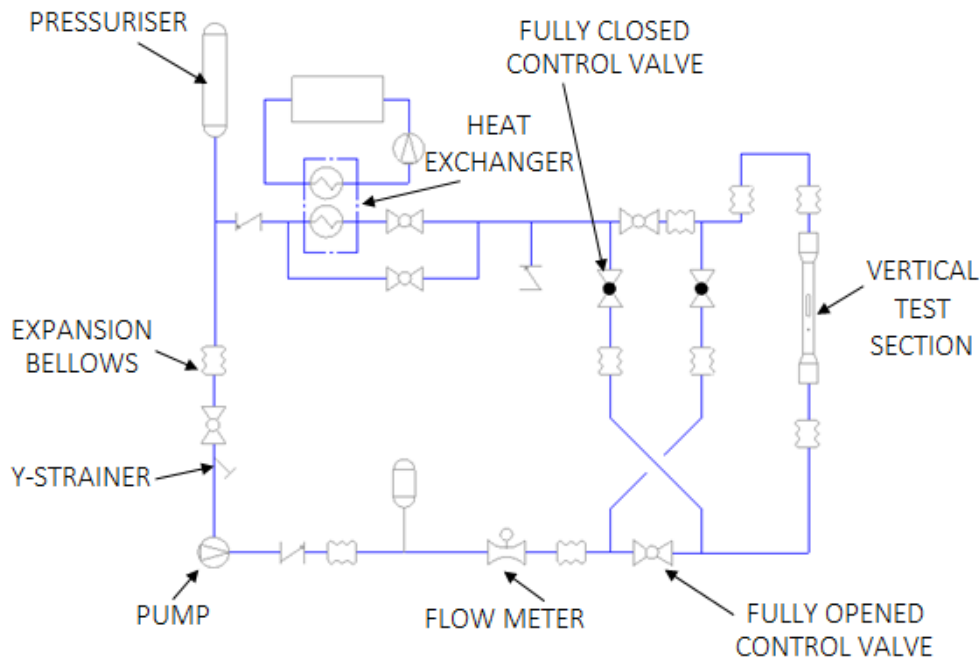
3.2.2   Test section

The removable panel, which can be seen in **Figure 10**, housed the test specimen and the important measurement probes. This allowed relatively simple input and extraction of the test specimen. The stainless steel removable panel was placed on the test section area and was secured by bolting it down. A gasket was used in-between to ensure a proper seal. The test section was rectangular in cross-section and was equipped with highly durable clear polycarbonate windows, which provided good viewing of the process inside. All the connecting cables necessary for the measurements were fed through the removable panel. An unwanted circumstance of this arrangement was that the power lines ran parallel to all the internal thermocouples and created a significant electro-magnetic field (EMF) distortion in the results. It was noted that this effect was directly proportional to the voltage increase in the heaters. A range of tests were done to investigate this effect and a set of calibrations was formulated to compensate for these unwanted effects.
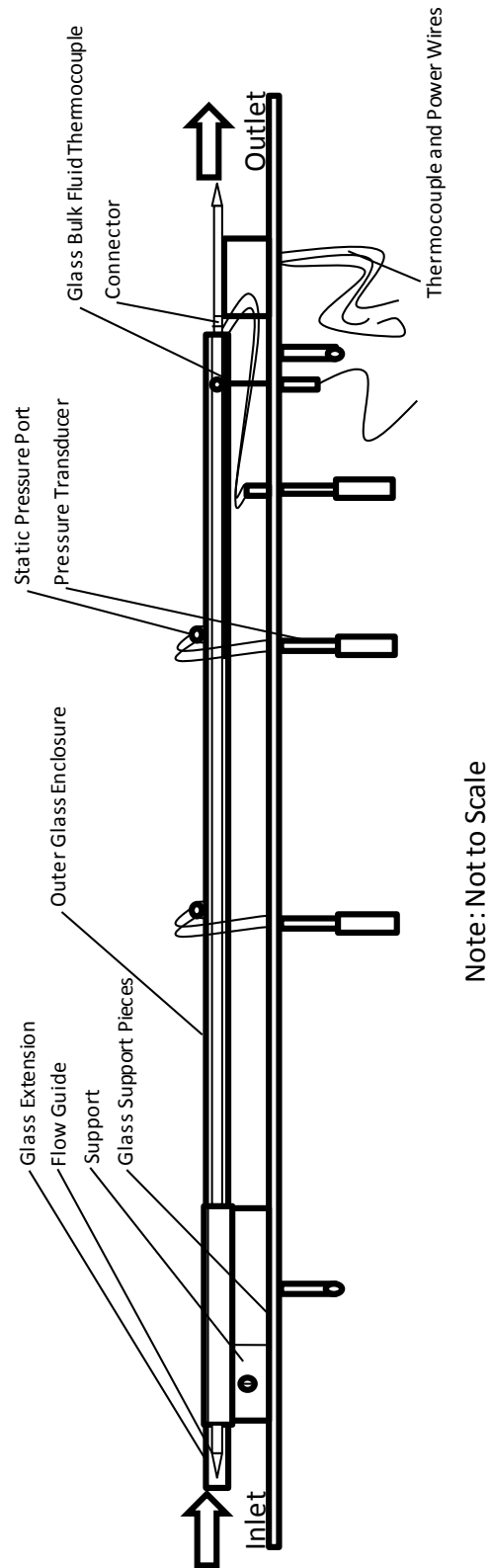
Figure 10 Removable panel full assembly

Plenum Box

Connecting Cables

Polycarbonate Glass

Camera
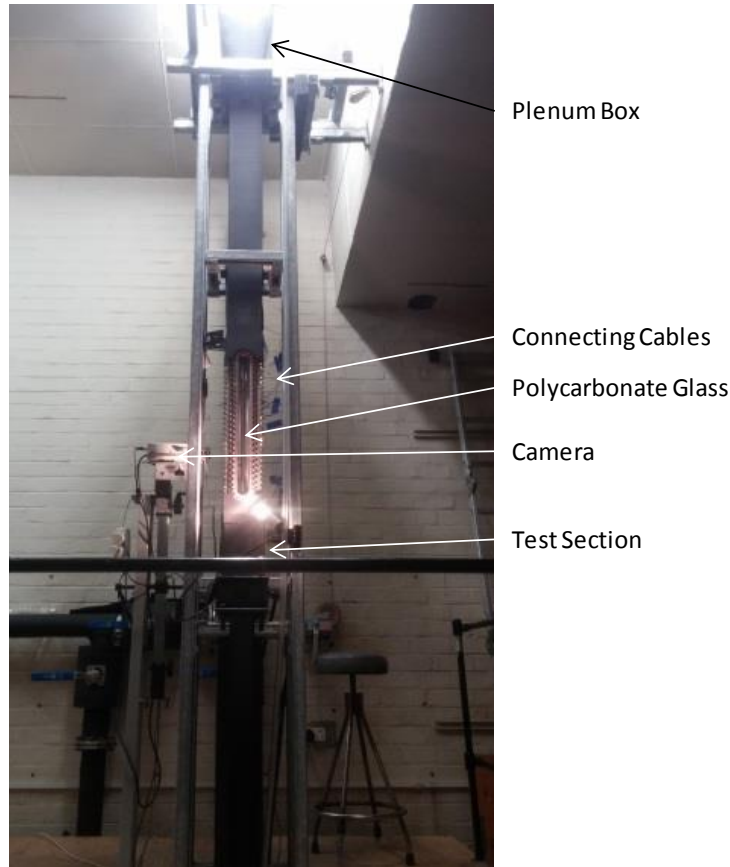
Test Section

Figure 11 Test section

The test section, seen in **Figure 11**, was 100mm x 100mm wide and 3m long. The large flow area meant that small pressure differences due to roughness could not be measured easily, which is why a glass enclosure was designed and used to better simulate the hydraulic diameter around a typical reactor fuel pin. The flow loop was maintained at an approximate pressure of 1.5 bar for the tests unless otherwise stated. Specially designed connectors and flow guides secured the test specimen to the removable panel and were used to lead the power and instrumentation cables to the outside of the loop pressure boundary. Supports were manufactured to successfully secure the rod specimen in line with the connectors. These supports were manufactured from polycarbonate. Small spider supports were 3D printed to keep the rod concentric in the glass enclosure. **Figure 12** provides a sketch of this glass enclosure.

24

Figure 12 Glass enclosure design

For a typical pressurised water reactor (PWR), the lattice pitch of a 17x17 fuel array configuration is 12.6mm [7]. The diagonal lattice pitch is therefore 17.82mm, as illustrated in **Figure 13**.
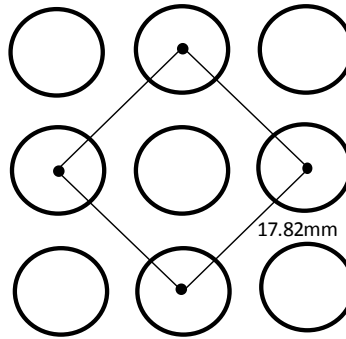
Note: Not to Scale

Figure 13 Fuel pin hydraulic diameter of a typical PWR

The area inside the square excluding the rod portions make up the hydraulic diameter. With the diameter of the Zircaloy® rod as 9.8mm, the hydraulic diameter is calculated as follows:

$$D_h = \frac{4A_c}{p} = 7.12mm$$

(29)

The glass inside diameter is calculated to be 16.92mm with the following hydraulic diameter relationship with the diameter of the Zircaloy®, in this case the inner diameter, measuring 9.8mm:

$$D_h = D_o - D_i$$

(30)

The outer diameter calculated is the inside diameter of the glass enclosure. Due to standard tube sizes, the final glass enclosure design had an inside diameter of 17mm. Uniquely designed support structures were designed and built. These were made from polytetrafluoroethylene (PTFE) due to its malleability and high melting temperature. To allow for flow settling, the glass was extended over the inlet support. This also achieved an entrance length of longer than 10 diameters. It is important to note the velocity of the water around the glass enclosure will be different to the water flowing inside the glass enclosure. The glass enclosure velocity is a critical aspect of this study and is discussed in detail throughout the rest of the dissertation. **Figure 14** depicts the full removable panel assembly.

26

Static Pressure Measurements

Connecting Cables Outlet

Glass Enclosure

Polycarbonate Window

Static Pressure Measurements

Test Specimen

Rod and Glass Concentricty Spider
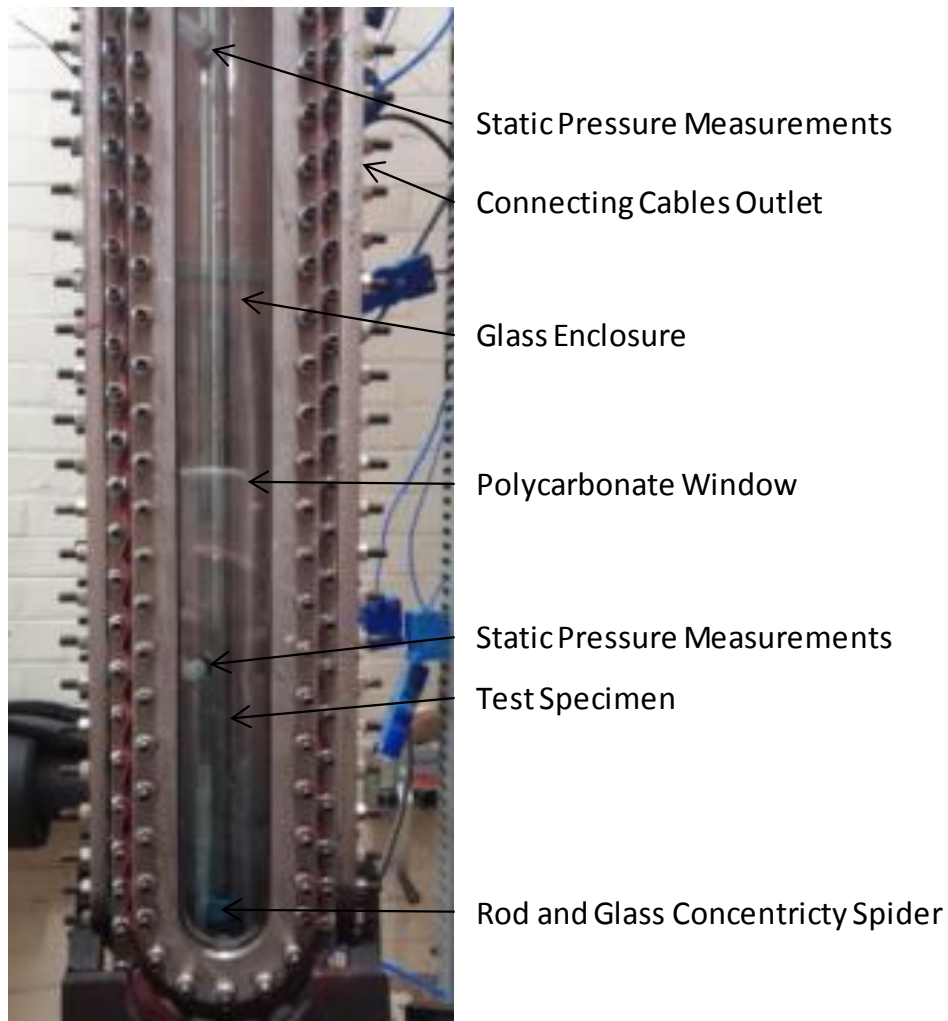
Figure 14 Final assembly of test section

The material used for the specimen was Zircaloy® and was obtained through the assistance of the South African Nuclear Energy Development Corporation (NECSA). The outer diameters measured 9.8mm and encased a resistance-type cartridge heater. The heater was supplied by a company called Swift and was rated at 2300W. It was 490mm long with an outer diameter of 8.2mm. The heater incorporated a J-type thermocouple placed in the centre (axially and radially) of the heater. The heater consisted of three different cartridges closely spaced with nichrome wire wrapped around a solidified magnesium oxide core, as illustrated in **Figures 15 and 16**. The close spacing was done in order to achieve a uniform heating distribution profile; subsequently, the ends had fewer windings. The power control of the heater was adjusted by an autotransformer outside the test rig room.

A crucial facet of the specimen measurement is the surface temperature. This is notoriously difficult to measure and is made more complex by the EMF effect mentioned earlier. Much consideration was given to what was the best strategy of measuring the surface temperature with initial designs including externally placed thermocouples on the specimen. These yielded unacceptable results as there were too many factors influencing the measurement area of the thermocouple. A solution was needed where the flow of the water would not affect the temperature readings and at the same time be as close as possible to the specimen surface. The final solution was to mill three long grooves on the heater itself and put the thermocouples in so as to place the whole heater with the thermocouples inside the Zircaloy® specimen. Three T-type thermocouples were inserted inside the Zircaloy®, one for each groove. The steel outer casing of the heater was approximately 0.9mm with the thermocouple junctions at 0.5-0.6mm in diameter depending on the size of the solder. The grooves that were milled were approximately 0.65-0.7mm in depth. They were placed 120 degrees apart on the circumference and at different lengths. The lengths were calculated in order to line up the thermocouples with the middle of the heater sections.

A thermal paste was used in-between the heater and the test specimen so that the heater could be inserted easily into the rod and act as a heat transfer medium, otherwise the air could drastically increase the insulation around the heater. The thermal paste assisted the heat in radially transferring to the tube.
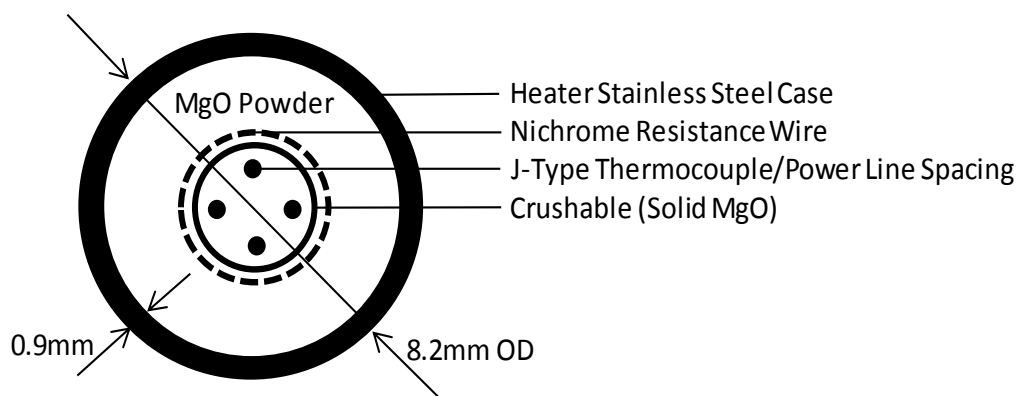
Figure 15 Heater Cross-Section
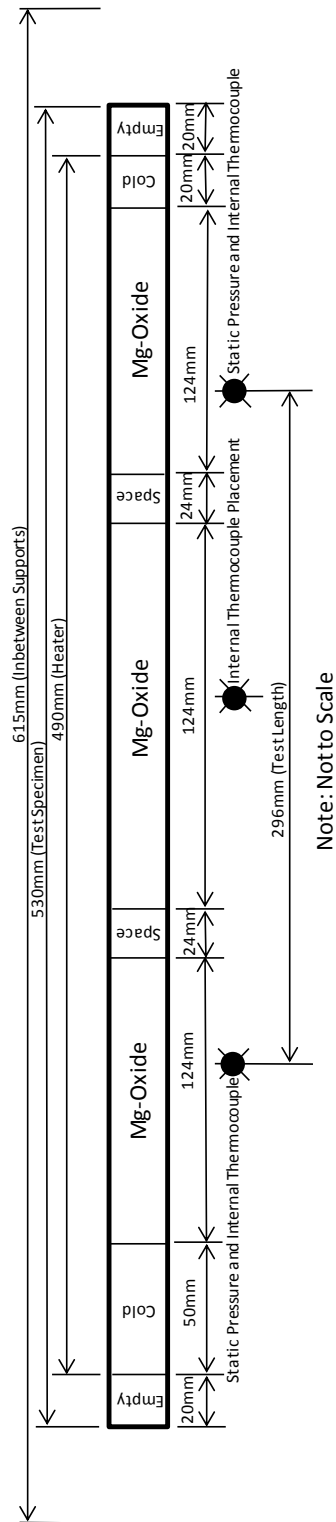
Figure 16 Test section breakdown and design

3.2.3 Test samples

Sandblasting was the chosen method for producing the surface roughness. Gero Engineering is a company that provides sandblasting services using four different materials as their grit [23]:

- mine sand;
- microblast®;
- sodabrade®;
- B60.

Throughout the rest of the dissertation, these four grit names are used to describe each respective roughened rod. The test sample and final experimental rod grits differed due to availability of the materials. The machinery name used for the sandblasting was not exactly known but the company representative supplied the specs of an equivalent blast pot. This unit was mobile and had a maximum capacity of 100 litres. It was pressure vessel certified and the machine is pictured in **Figure 17** [24].

Figure 17 Sandblasting equipment used

The sandblasting was done at 2.5 bar, which is considered a low pressure. Test samples of Zircaloy® about 6cm in length were used to determine whether the sandblasting would be feasible. Five initial sample test pieces were sandblasted with the different materials and by

30

touch they all felt different with regard to the surface textures. The tubes were mounted over another rod to ensure stability during the process.

The final rods were sandblasted with the length cut to operational specification required for the flow loop. Attention was given to the uniformity of the sandblasting to avoid a great variation in roughness along the tube. The method of mounting the tubes over another rod from the test samples was used again to ensure stability.

3.2.3.1 Mine sand

The mine sand that was used for the grit was general sand found at a mine and can be seen in **Figure 18**. Due to this informal nature of the grit, an X-ray diffraction (XRD) was done to verify what the mine sand was composed of. The Faculty of Natural and Agricultural Sciences' XRD and XRF facility conducted the XRD, which was done by a trained professional. A sample of the mine sand used by Gero Engineering was used. Three material classifications were found, namely quartz, pyrophylite and muscovite or illite. Muscovite and illite have the same structures; therefore, making it improbable to properly define. Muscovite and pyrophylite are clay minerals. Quartz was found to be dominant with a 92.72 weight percentage. For the test results, see **Appendix B** [25].

Figure 18 Mine sand

3.2.3.2 Microblast®

Microblast® is a natural mineral grit and can be seen in **Figure 19**. Microblast® is considered efficient due to its ability to be recycled. It mostly consists of almandine [26].

Figure 19 Microblast®

3.2.3.3 Sodabrade®

Sodium bicarbonate, also called Sodabrade®, is used for cleaning many surfaces due to its ability to remove hydrocarbons [26]. Sodium bicarbonate can be seen in **Figure 20**.

Figure 20 Sodabrade®

3.2.3.4 B60

B60 is a specially formed grade of mineral slag by the company Blastrite used for specific surface finishes where abrasive techniques are needed [26]. The chemical composition is mainly silicon dioxide and iron(III) oxide comprising 73% of the weight along with 15% of magnesium oxide. B60 can be seen in **Figure 21**.

32

Figure 21 B60

3.2.4   Surface roughness measurement

The selected method to measure the surface roughness was a probe called the Elcometer 124 thickness gauge and has a range of 0-5mm in roughness measurement [27]. The scale resolution is 2µm which serves to read an accurate roughness [27]. The AFM method was initially used to measure the roughnesses. An extensive range of tests were done using the AFM to ensure a decent average but this method proved to be very erratic with a large standard deviation. The Elcometer 124 thickness gauge provided more steady results.

Table 1 Surface roughness results

	Ra (µm)
Plain	21
Mine sand	40
Microblast	96
Sodabrade	27
B60	50

Table 1 summarises the roughness results for each rod. As with any experiment, there are possible reasons for errors and inherently any experiment has its flaws, which can affect the final results. The possible limitations or errors were:

- The tip could be limited by its height range when travelling over peaks and valleys, therefore, making rough samples slightly smoother than what they were in reality.

33

- The roughest tubes were the hardest to test due to their complex surface nature.

- Any loose particles on the surface could disturb the experiment.

- All the rods were sandblasted as uniformly as possible. The Sodabrade®-sandblasted Zircaloy® had a unique roughness relative to the rest because the peaks and valleys were vastly spread apart.

3.2.5 Instrumentation

It is vital to know how all the instrumentation pieces behave before they are used. This means calibrating them in conjunction to known and verified measurements. The next section deals with the calibrations of all the relevant measuring instruments.

3.2.5.1 Pressure transducers

Wika supplied all the pressure transducers and they came calibrated. Calibration certificates were supplied and used in the data processing procedures. The pressure transducers measured static pressures and consisted of two different types. One measured in the range of 0-2.5 kPa and the other measured in the range of 0-10 kPa.

3.2.5.2 Thermocouples

Wika provided T-type sheathed thermocouples as well as Pt100 thermocouples [28]. The Pt100 thermocouples came precalibrated at $1\,°C$ but the T-type sheathed thermocouples were not and were calibrated using ethylene-glycol in a temperature-controlled thermal bath [28]. The bath was heated to $125\,°C$ from $50\,°C$ at $5\,°C$ intervals. This is a wide range for good accuracy. Readings were taken at each interval after approximately five minutes to allow steady-state conditions and therefore decrease the inaccuracy. A linear regression model was used to plot the calibration curve, which would be implemented to ultimately calibrate the T-type thermocouples. The T-type thermocouples were used to measure the bulk fluid temperature at the inlet and the outlet of the removable panel as well as the bulk fluid temperature on the outlet side inside the glass structure. The Pt100 thermocouples were used to measure the temperatures at the pressuriser, heat exchanger and the inlet and outlet of the pump.

The thermocouples used to measure surface temperature were made from T-type thermocouple wire soldered together at the junction. The thermocouples were calibrated in a bath of water heated up to boiling temperature and cooled down overnight. This provided a long period, which gave many data points. The same linear regression model was used to get to a calibration curve for each of the thermocouples.

34

3.2.5.3 Flow meter

The venturi and the differential pressure transducer were calibrated while coupled together at Endress+Hauser.

3.2.5.4 Power supply

An autotransformer in connection with a solid-state relay was used to control the power input to the system. The relay varied the fixed power supply of 220V at a frequency of 50Hz. It effectively varied the energy content in the sinusoidal wave by a clipping process but the overall frequency stayed the same. The power supply was AC, while the pressure transducers were powered by DC power.

3.2.5.5 Data capturing

For safety reasons, a control area was constructed outside the test rig room and facilitated the author to control most experimental parameters from outside the room at a control desk. A data acquisition system (DAQ), Agilent 34970A, was used to log all the test data through National Instrument's Labview software on the computer. The Labview software was used to implement all calibrations so that all real-time readings were what they were meant to be. A television screen next to the computer gave a visual of the test section area where a camera was placed. Pressure could be adjusted with a series of valves and the system mass flow rate could be controlled by the VSD controls. The following measurements were taken and recorded in each test:

- scan step period;
- inlet and outlet pressure of the test section;
- heater voltage and current;
- embedded heater thermocouple;
- inlet and outlet bulk fluid temperatures of the test section;
- internal interface temperatures;
- mass flow rate;
- flow velocity.

These measurements exclude fluid properties calculated by empirically derived formulas [29]. This information can be found in **Appendix A**.

3.3 Flow loop validation

The flow loop was newly built when the author conducted the tests. The author was the first to officially use the flow loop for experimental purposes. The flow loop characteristics were still unknown when the experiment was started and therefore many tests were required to achieve some understanding. Validation was done with particular focus on the surface temperature, in relation to the heater performance, as well as the pressure. These two measurements formed the basis of the problem statement, which made it vital to understand. All validation tests were done with a plain rod and three embedded thermocouples were referred to as long, medium and short relative to the distance from where they entered next to the heater.

3.3.1 Mock flow loop

Using the flow loop is time consuming and complex with regard to the installation of the test specimen. This made initial validation tests difficult to execute. Due to the complex nature of the flow loop, a mock flow loop was designed and built. After basic functions of the flow loop were concluded to be working, all the base pressure and temperature validation tests were done on the mock flow loop. The mock flow loop, seen in **Figure 22**, consisted of a tank filled with water and was connected to a pump. This simulated the basic function of the large flow loop under atmospheric conditions.
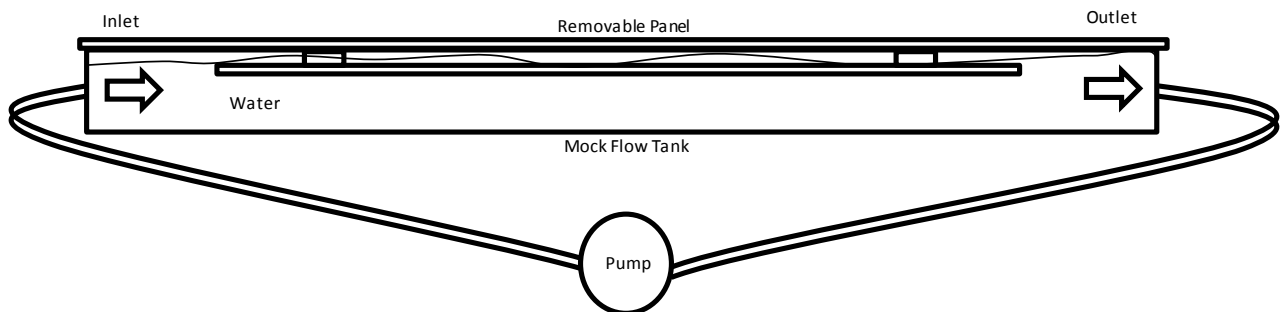
Note: Not to Scale

Figure 22 Mock flow loop

3.3.2 Heat input measurement

Initial tests were done to validate the basis of the electrical input readings. A voltmeter and ammeter were connected to the system while the heat was ramped up. The readings on the voltmeter and ammeter did not correlate well with the readings given by the Labview software. A test was done in order to find out how the power behaved compared with a multimeter with a

36

known accuracy and a calibration curve was produced in order to properly amplify the results being read. An oscilloscope was used to check whether the power factor and the result yielded that it was unity and therefore no power factor correction was necessary in the processing of the data.

3.3.3 Surface temperature measurement

The following two important factors were investigated in surface temperature measurement:

- The physical placement of the thermocouple was made more complex by the water flow and tight fit of the heater in the test specimen.
- The EMF effect resulted from the power lines running so close to the thermocouples.

The first set of initial validation tests was done on a different set of embedded thermocouples from the ones used in the final validation tests and final tests. The first set behaved similarly in many ways even though the methods implemented were different. This laid the foundation for accepting the final behaviour of the embedded thermocouples. The thermocouple behaviour was at times very erratic and unpredictable.

3.3.3.1 Thermocouple placement

Initially, the thermocouple placement idea was to place them directly on the surface while having the thermocouple junction touching the surface. This method was unsuccessful because the length of the thermocouple acted as a cooling fin as the water flowed by. A silicone tube was placed over the thermocouple in an attempt to eliminate this unwanted effect as well as a rubber boot at the junction to better guard the point of measurement. This too was unsuccessful due to the cooling of the water flowing past.

The only other pragmatic solution was to place the thermocouples inside, in-between the heater and specimen. In this way, the flow did not affect the readings and the thermocouples were as close to the surface as possible. The disadvantage of this method was the fact that the power lines were parallel to the thermocouples. This created an EMF effect disrupting the thermocouple readings [30]. Normally, this can be rectified by implementing shielding material covering the thermocouple but the tight fit of the heater made this solution unfeasible. The thermocouples used were the thinnest obtainable at the time.

The thermocouples tracked each other well when the heater was turned off but strayed when the heater ramped up. This could be due to the EMF effect or the lack of uniformity of the

heater. This led to the necessity of an EMF correction factor and a further investigation into the uniformity of the heater.

3.3.3.2 Heater uniformity

A test was done by bending a piece of copper drilled and impregnated with a thermocouple. The copper saddle thermocouple was moved along the test section while the heater was switched on and was compared with the internal built-in thermocouple of the heater, they tracked each other well and demonstrated a decent uniformity of the heating coils. From observations, the internal thermocouple was not generally affected by the EMF and thus was used to compare the copper saddle. The internal thermocouple was placed in the heater by the Swift company and was not relied upon in the final tests as there were no calibrations for the thermocouple. The uncertainty of its exact placement and calibration made it unreliable but the internal thermocouple was used as a base indicator. The results can be seen in **Appendix D**.

3.3.3.3 EMF correction

A conclusion on the effect brought about by the EMF disturbance was achieved by doing two different tests in the mock flow tank. The one test involved gradually heating the water with a separate immersion heater placed in the tank. This allowed the heater to be switched off while increasing the temperature of the fluid. The pump was switched on to ensure even circulation of the heated water. As can be seen in **Appendix D,** the temperatures all followed each other well. There was very little discrepancy in the temperature reading results. The second test was done with pool boiling conditions where the pump was switched off. The power was increased and dropped back down to zero. The next round was ramped up higher than the previous time and brought back down to zero. This was done to cover a large range. The temperatures once again followed each other very well. These tests proved that the thermocouple method implemented did work but a solution was necessary to compensate for the EMF for the heater when it was in use.

To correct the EMF effect, a strategy was devised in order to quantify the effect. In the mock flow loop with the pump running, the heater would be increased at set intervals. The data was then analysed with attention to the moment the heater was increased and the temperature differences were calculated and plotted against the voltage. This was put on a graph with a linear regression line drawn. The tests were repeated five times and two separate sets were done. One set of tests was done at approximately 10V intervals and the other at approximately 25-30V intervals. The five tests were averaged in both cases. The logic behind this method was

that the instantaneous temperature jump was the result of the EMF effect and not necessarily the increase in voltage, this could then be used to subtract from the reading to get a more accurate temperature measurement. Further inspection of the results found in **Appendix D** was that the gradient of the 25-30V was greater than the 10V tests. This was expected due to the fact that the voltage increase now had two predominant effects, the EMF and the temperature spike. The voltage jumps used in the final tests were roughly 50-60V. In theory, the 10V correction equations would be suitable in correcting the temperature measurements for the final results because the 10V tests more accurately detailed the EMF effect. This correction method was implemented with the assumption that the rate of change due to the EMF was constant along the whole voltage range.

These tests were done with only the long and short embedded thermocouples because the middle thermocouple was malfunctioning. The long and short embedded thermocouples refer to the outlet and inlet thermocouples, respectively. This could always be a possible pitfall because the method of inserting the thermocouples posed operational risks such as snagging the wires. The middle thermocouple was eventually averaged between the long and short thermocouple, which was a good assumption based on previous thermocouple behaviour. To avoid a ground loop in the final tests adversely affecting the thermocouple measurement, connectors were made from polycarbonate instead of stainless steel [30]. These connectors were manufactured pieces designed to hold the sample specimen in line with the end flow guides. Polycarbonate has a high melting temperature for a plastic and therefore met the necessary requirements.

3.3.4   Pressure measurement

The static pressure for the inlet and outlet of the test section was validated by venting the loop to atmosphere and stopping the pump. The flow loop was filled with water. The atmospheric pressure was recorded to be 87.5 kPa by using a Kestrol airflow meter which is a handheld device with a fan. **Equation 32** was used to calculate the expected pressure readings and was compared to what was measured by the pressure transducers:

$$P = \rho g H$$

(31)

The outlet pressure reading had a percentage error of -1.65% and the inlet was -1.19%. Data is provided in **Appendix D**.

3.3.5   Water quality

3.3.5.1   Spectroscopic infrared water tests

Spectroscopic tests are very useful in analysing the nature of a substance at micro level and were used to explore the quality of the water used in the loop during initial testing. Two sets of clean and used distilled water along with two sets of deionised water were tested to better illustrate how pure the water used in testing really was, as can be seen from the results summarised in **Appendix B**. All samples matched each other very well and the wavelength spikes indicated that virtually no contaminants were found in the water. All the spikes indicated the expected O-H bonds. Whether the distilled water was fresh or pre-used in the system, the quality did not change dramatically.

3.3.5.2   Dissolved oxygen measurements

Dissolved oxygen measurements were taken to indicate how much oxygen was present in the water. This dramatically affected boiling regimes [14]. The HACH HQ30d is a handheld meter used to measure critical water quality parameters and was used to measure the dissolved oxygen. The general norm for tap water is anywhere between 5-9 mg/L. Water extracted after the final tests for the plain rod measured 6.45 mg/L. Water extracted after the final tests for the rough rods read 6.48 mg/L.

3.3.6   Glass Enclosure Velocity

This part of the experimental process was done last after all the main tests were conducted as there were uncertainties about the velocity of the water flowing inside the glass enclosure. This velocity is difficult to measure due to the the space limitations. The velocity is greatly affected by the roughness and is therefore vital in establishing the heat transfer nature of the rod. Apart from the main tests a set of velocity validation tests were conducted. Initially it was postulated that a dynamic pressure probe at the inlet of the test section would suffice in concluding the velocity flowing through the test section but this method yielded very high scatter and inconsistencies and was deemed inaccurate for validation purposes.

It was decided to force all of the water to flow through the glass enclosure and study the results to accurately validate the velocity of the water. To ensure all the water flowed through the glass enclosure two flow concentrators were 3D printed and the black pieces seen in **Figure 23**. One piece is for the inlet and the other for the outlet. A separate spacer was manufactured to guarantee the tube stays concentric to the rod specimen. The glass enclosure was replaced

40

with plexi glass for safety reasons. The surface roughnesses are very similar, the glass was measured to be $25\mu m$ so the assumption was made that the plexi glass was similar and would not affect the fluid velocity significantly.

Figure 23 Inlet and outlet flow concentrators

The ΔP_{flow} was calculated by subtracting the outlet test section pressure from the inlet test section pressure and then subtracting the static pressure head. The 6.4kg/s tests had values of ΔP_{flow} larger than those of the 3.2kg/s tests, as expected. A closer look would reveal an approximate squared relationship between them, which correlated well with the pressure and velocity relationship in the incompressible steady flow energy equation, $P \propto V^2$. The difference in ΔP_{flow} at 6.4kg/s was roughly 50Pa. This validates that the loop was running in accordance with basic fluid flow laws and further investigation could take place.

After all the main tests were done a variety of pressure drops were recorded. This was because the system mass flow rates of 0kg/s, 3.2kg/s and 6.4kg/s were used. The velocity of the water flowing inside the glass enclosure was calculated using the form of the energy equation found in **Equation 37**. **Figure 24** details the two scenarios that were dealt with. In number one, found on the left hand side, the water has two paths flowing around the glass enclosure as well as through it. This is the scenario of all the main tests where the heaters were ramped up. In number two the water is forced to flow only through the glass enclosure by means of the flow concentrators. This is the scenario of the velocity validation tests. With these two scenarios the hydraulic diameter is constant between the height the pressure drop is read so the only

necessity in comparing the main test results to the velocity validation test results is matching the pressure drops. This is why the velocity validation tests were simply done by ramping up the pump from zero all the way up in small increments in order to ensure steady state reading for a range of velocities.

The velocity validation test results provide an array of pressure drops as well as the readings for the flow rate recorded from the venturi. These recorded flow rates were used to calculate the velocity inside the glass enclosure by using the relation:

$$Q = A_{venturi}V_{venturi} = A_{glass\ enclosure}V_{glass\ enclosure}$$

(32)

By matching up the pressure drops from the main tests with the pressure drops from the velocity validation tests a velocity could be read up that was calculated from the venturi.
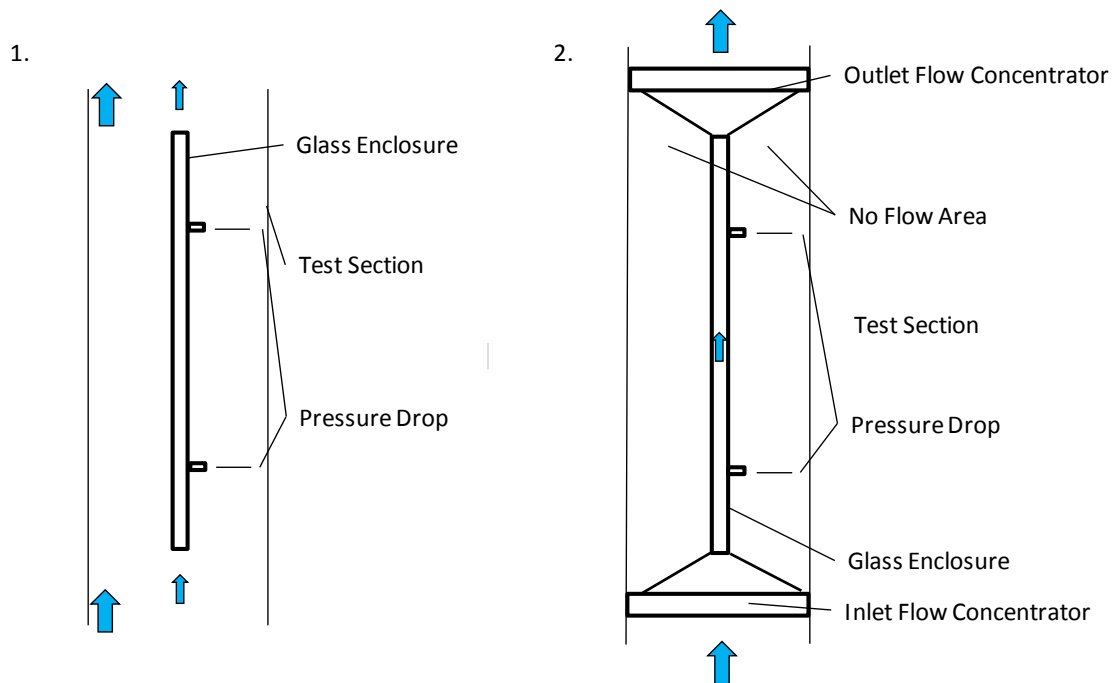
Figure 24 Velocity validation setup scenarios

3.4 Experimental procedure

This section details how all the final tests were done and what guidelines were followed in order to maintain consistency and integrity. Initially, the task was to insert the surface temperature thermocouples firmly into the grooves of the heater that were milled out. It was important to note whether the soldered junction protruded since this would impede the Zircaloy® from slipping

over it. Once the thermocouples were in place, a thermal paste was generously applied to the entire heater, this had the function of filling the air gap between the heater and the Zircaloy®. The heater was then slowly inserted into the Zircaloy®. All the wires leading out of this assembly were then led out through the hollow support through the connector to the outside of the test section. The outer-glass section had to be slipped over the Zircaloy® before everything was tightened. The assembly was then connected to the other end support and fastened with the connectors in place. To avoid the glass from touching the Zircaloy®, the glass support structure was then connected to keep the glass concentric to the Zircaloy® rod. The inner-glass bulk fluid sheathed thermocouple could then be positioned along with the total pressure probe. The total pressure probe was not used for all the tests as it was a late addition. The assembly on the removable panel was placed on the test section and bolted onto the test section. Prior to insertion, a test was done in the mock flow loop to check for leaks.

The system was then filled with water. The loop was filled with water by using compressed air in the storage tank. This transferred the water into the loop. Some of the vents found at high points were kept open to keep a constant pressure and to alert the user that the loop was full when water started overflowing. Before any tests commenced, the bulk fluid temperature had to be raised and this was done by switching on the preheaters and the pump. The flowing water increased in temperature to the desired starting point.

3.4.1 Start-up procedure

The bulk fluid had to be heated to its starting point, which was decided to be 30 ℃. The pump was on at this point to circulate the heated water around the system. There were a few variations above this for some tests. Due to the fact that the heat exchanger did not work reliably at this point, the system was not always able to cool down quickly enough. As the tests ran for each rod, the bulk fluid increased in temperature for each repetition ending off at approximately 40 ℃. This routine was closely followed for uniformity in the tests. While the water in the flow loop was heating up, all the readings were checked for proper operation. It was important to ensure that the surface and bulk fluid temperatures as well the inner-glass and test section pressures were working before continuing. A total pressure probe was only added after the second rod. Once the flow loop was stable, testing could commence.

3.4.2 Data capturing

Due to the number of rods tested and the nature of the measurements, many repetitions were conducted. A testing procedure was devised and followed. When the pump was switched on,

the flow direction was always upwards making the top of the test section the outlet. There were five rods with varying roughnesses including the smooth Zircaloy® used in industry. Each test would be repeated six times. The first test was not included in the analysis because this was the deaeration repetition effectively supplying five repetitions of data. The working pressure was 1.5 bar and was set as the approximate average between the inlet and outlet static pressures of the test section. The heat input was increased at 20% intervals on the autotransformer and left to settle for roughly three to five minutes. This heat input process was conducted at three different system mass flow rates, namely 0kg/s, 3.2kg/s and 6.4kg/s. This provided an array of results covering many different heat transfer and fluid mechanics combinations.

The glass enclosure velocity tests were then performed after the main heating analysis tests. With the plain rod used the heaters were switched off and the system pressure set to the same 1.5 bar the system mass flow rate was increased incrementally and left to settle. This was done in increments as small as possible to ensure a detailed range. With the system mass flow rate increasing the pressure inside the glass enclosure increased. This test was repeated three times. The pressure drops from the previous original tests were cross referenced with the new set of data. This was possible because the hydraulic diameters from the original tests was the same as for the these validation tests. The corresponding velocities from the venturi, which is situated outside of the main test section area, were noted and used to calculate the glass enclosure velocities by means of taking the areas into account. The average pressures of the final tests were used to look up what the velocity was. The pressure drop used was the pressure drop due to the flow which was calculated by removing the static head component.

3.4.3 Data reduction

All calibrations and corrections were implemented and checked including the EMF normalisation method. Heating up of the Zircaloy® was done by Joule heating. Joule heating in this case involved passing an electric current through the wire with the resultant heat produced being the desired effect.

3.4.3.1 Pressure drop

The static pressures measured were subtracted from each other to describe the pressure difference in the test section between the inlet and the outlet:

$$\Delta P_{measured} = P_{inlet} - P_{outlet} \tag{34}$$

with:

$$\Delta P_{flow} = \Delta P_{measured} - \Delta P_{head} \tag{35}$$

where:

$$\Delta P_{head} = \Delta P_{measured} \; at \; 0kg/s \tag{36}$$

3.4.3.2 Fluid analysis

It is important to note that the fluid properties were taken by the Labview software at the average temperature between the inlet and outlet of the test section. These were mixed mean temperatures. In the analysis, the fluid temperature was analysed between the inlet of the test section and the inner-glass bulk fluid temperature at the outlet. Essentially, the Labview software properties were effectively a small percentage above the inlet bulk fluid temperature.

Due to there being no flow measuring device inside the glass enclosure it is calculated from the measured pressure drop by analysing the energy equation for incompressible steady flow [5]. Assuming the velocity is constant throughout the tube the kinetic energy terms can be cancelled and the velocity inside the glass can be arranged as:

$$V = \sqrt{\frac{2D_h(\Delta P - \rho g \Delta Z)}{\rho f L}} \tag{37}$$

The Reynolds numbers were calculated:

$$Re = \frac{\rho V D_h}{\mu} \tag{38}$$

assuming the average roughness as the absolute roughness:

$$\frac{\varepsilon}{D_h} \tag{39}$$

The Moody chart was used to obtain the Darcy friction factor through the Haaland formula:

$$\frac{1}{f^{\frac{1}{2}}} \approx -1.8 \log \left[\frac{6.9}{Re_d} + \left(\frac{\frac{\varepsilon}{D_h}}{3.7} \right)^{1.11} \right] \tag{40}$$

3.4.3.3 Heat transfer

The embedded thermocouple was very close to the surface but the thermal conductivity of the Zircaloy® had to be accounted for when calculating the surface temperature. The conductivity

45

changed with temperature, the average between 300K and 400K was used at $k = 13.7\frac{W}{m}.K$ [31]:

$$Q = kA\left(\frac{T_1 - T_2}{L}\right) \tag{41}$$

The surface temperature was calculated from:

$$T_s = T_{embedded} - \left(\frac{\frac{q}{A_s}L}{k}\right) \tag{42}$$

with the surface area calculated from:

$$A_s = 2\pi r l \tag{43}$$

Two ΔT definitions were used to articulate the heat transfer. The first was the general heat transfer between the surface and the bulk fluid:

$$\Delta T = T_s - T_f \tag{44}$$

and the second for boiling:

$$\Delta T_{boiling} = T_s - T_{sat} \tag{45}$$

$\frac{q}{A_s}$ was used to empirically calculate the heat transfer coefficient:

$$h = \frac{\frac{q}{A_s}}{\Delta T} \tag{46}$$

with the Nusselt number:

$$Nu = \frac{hL_c}{k} \tag{47}$$

3.4.3.4 Roughness optimisation

If a rougher tube should assist in improving the heat transfer, then from the Darcy Weisbach equation it is expected that the associated pressure drop will increase too. A higher pressure drop will in the end translate into higher running costs for the plant. A comparison study was done to verify what the best solution would be. Due to the limitations of the pressure analyses, the pump head due to friction was used to communicate the percentage increase brought about by the roughened rod assuming the rod in question had an improved heat transfer coefficient.

46

The Colburn J-Factor was calculated in order to normalise and compare the roughness results:

$$j = \frac{Nu}{RePr^{\left(\frac{1}{3}\right)}} \tag{48}$$

3.5 Uncertainty analysis

The uncertainty analysis was implemented for all the instruments used along with other important calculated parameters including the pressure drop, heat transfer coefficient and EMF effect. Moffat [32] proposes an analytical analysis for an uncertainty analysis, which was used in this research to scientifically quantify the possible errors experienced throughout these tests. **Tables 2** is a summary of all the uncertainties and all derivations is shown in **Appendix F**. The heat transfer area error used in the final uncertainty results was:

$$\delta A = 4.5352E - 5\ m^2, (0.31\%\ Error)$$

The flow pressure drop error used in the final uncertainty results was:

$$\Delta P_{flow} = 2598.08Pa, (1.73\%\ Error)$$

Table 2 Calculation uncertainties

	Maximum uncertainty (%)
Heat flux, $\frac{q}{A}$	10.67
Heat transfer coefficient, h	8.07
Nusselt Number, Nu	8.23
Velocity, V	30.15
Reynolds number, Re	19.60
Colburn J-Factor, j	21.12

3.6 Summary

The flow loop was a new design installed in the Thermo-flow laboratories of the University of Pretoria and like all technological endeavours could be improved upon. This meant clarifying what the problems were and finding solutions for them. Procedures had been established along with strategies to compensate for these unavoidable interferences. The uncertainty analysis yielded satisfactory results and must be kept in mind when analysing the results.

4 Results

4.1 Introduction

The nature of a comparative study is that many repetitions are necessary in order to provide repeatability. Two sets of tests were done on each of the five rods. The first set of tests was a heating analysis where the heater input was periodically increased from 0% to 100% in 20% intervals approximately every three minutes. After reaching full power, the power was switched off and the flow velocity (i.e., the linear flow velocity of the coolant adjacent to the heated rod) increased in order to repeat the test. Three system mass flow rates were tested, namely 0kg/s, 3.2kg/s and 6.4kg/s. Each test with all the velocities lasted approximately 45 to 55 minutes and was repeated six times for each rod. The first repetition was only for deaeration and was not used in the data reduction and processing. The second set of tests involved the flow concentrators to better validate the glass enclosure velocity.

The surface temperature was averaged across the entire rod as well as the repetitions and heat input range. The heat transfer coefficient was averaged from all the repetitions. The temperature difference to the flowing water increased, as expected, along with the heat input increase resulting in a relatively constant heat transfer coefficient.

4.2 Observations

The observations shown in **Table 2** were taken at the short embedded thermocouple and was recorded directly from Labview software without the EMF correction and could therefore be used for comparison purposes only. The velocity boundary layer could be noticed at times close to the surface and was seen to be only a few millimetres in thickness. For all rods, each stage of heating was noticed at a higher surface temperature, which was expected except for Microblast®. The plain rod was noted having far less churning on the surface compared with that on the rougher rods, which was to be expected. When bubbles formed on the surface, they seemed to occur at specific places in a continuous stream, which was interesting because bubble formation theory describes the best location for bubbles to form originating from the correct cavity sizes and peak angles. The higher the system mass flow rate, the more agitation was observed. It is important to note the stages of heat transfer. "Rays of heat" were noticed, which pointed to convective heat transfer and bubbles were noticed occurring from when they collapsed to where the surface tension was strong enough for them to grow and depart from the

surface. Referring to the work of Collier and Thome in **Figure 4,** this form of bubble formation was strong enough to prove that the incipience of nucleate boiling was achieved [10].

Table 2 Test observations

Temperatures noted at Outlet Thermocouple (Degrees Celsius)	**Convection heat transfer**	**Bubbles form and collapse**	**Bubbles form and depart**	**Nucleate boiling**
Plain	*Comment: Not many bubbles*			
0kg/s	100		115	120
3.2kg/s	105		128	
6.4kg/s	110	115		
Mine sand	*Comment: Dramatic increase in bubble formation compared with plain rod, much churning at high velocities*			
0kg/s	70		90	150
3.2kg/s	100		140	170
6.4kg/s	90		120	
Microblast	*Comment: Dramatic increase in bubble formation compared with plain rod but less than mine sand*			
0kg/s	100		115	
3.2kg/s	80	95	125	
6.4kg/s	75	95		
Sodabrade	Comment: Not as violent as mine sand and microblast			
0kg/s	60	80	95	160
3.2kg/s	80	95	125	
6.4kg/s	90	95		
B60	Comment: Not as much churning as microblast but the same as mine sand			
0kg/s	87	95	115	170
3.2kg/s	90	125	181	
6.4kg/s	92			

Pool boiling (i.e., at 0kg/s system mass flow rate provided the most visible bubble formation as can be seen in **Figure 25 and Figure 27**. At 3.2kg/s, **Figure 26 and Figure 28**, and 6.4kg/s, the bubble formation was not very visible as the flow boiling dragged the bubbles away as soon as they were formed.

Figure 25 Plain rod at 0kg/s with full power input (170000 $\frac{W}{m^2}$)
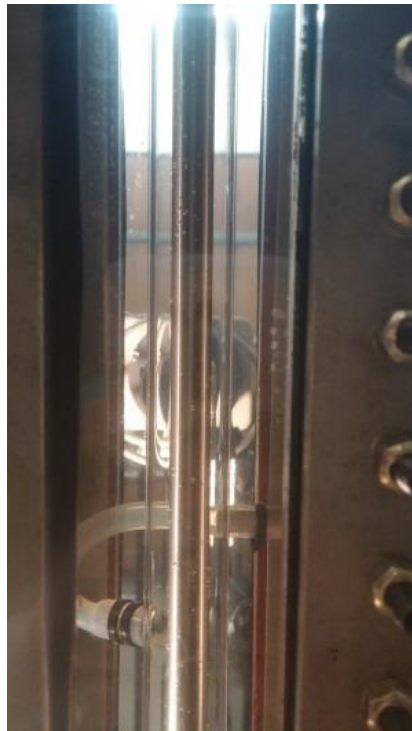
Figure 26 Plain rod at 3.2kg/s with full power input (170000 $\frac{W}{m^2}$)

Figure 27 B60 rod at 0kg/s with full power input (170000 $\frac{W}{m^2}$)

Figure 28 B60 rod at 3.2kg/s with full power input (170000 $\frac{W}{m^2}$)

4.3 Velocity

The velocity validation tests, see **Section 3.3.6**, proved successful in confirming the velocity of the water flowing through the glass enclosure. The high scatter in the results means a definitive answer could not be concluded but that a range of velocities would serve to back-up the calculated velocities. The scatter is due to the pump not being designed to operate at such low rpms and the inherent pressure oscillations of the system. The calculated velocities for the main tests using the energy equation yielded 0.2 m/s and 0.48m/s for the 3.2kg/s and 6.4kg/s system mass flow rates respectively. At 3.2kg/s the pressure drop due to flow is 0.00046 bar and at 6.4kg/s it is 0.00203 bar. Comparing these calculated velocities with the velocities from the velocity validation tests, it is noted to be well within range therefore validating the calculated velocities. **Table 3** shows the average water speed through the glass enclosure along with its Reynolds number.

Table 3 Velocities and Reynolds numbers

	3.2kg/s	6.4kg/s
Calculated Velocity (Average Over Rods, m/s)	0.36	0.55
Calculated Reynolds Number (Average Over Rods)	3950	5988

4.4 Pressure drop and heat transfer

The pressure drop versus Reynolds number can be seen in **Figure 29**. For forced convection with water flowing in pipes, the expected heat transfer coefficients are in the range of $250 - 12000 \frac{W}{m^2.°C}$ [7]. When dealing with boiling water flowing in a tube, the expected range is $5000 - 100000 \frac{W}{m^2.°C}$ [7]. The results in **Figure 30** correlated well with expected values in the nuclear industry. It can be noted that the plain, Sodabrade® and B60 rods had the best heat transfer rates. Therefore, it was necessary to analyse which of these had the best heat transfer coefficient and pump head due to friction trade-off.
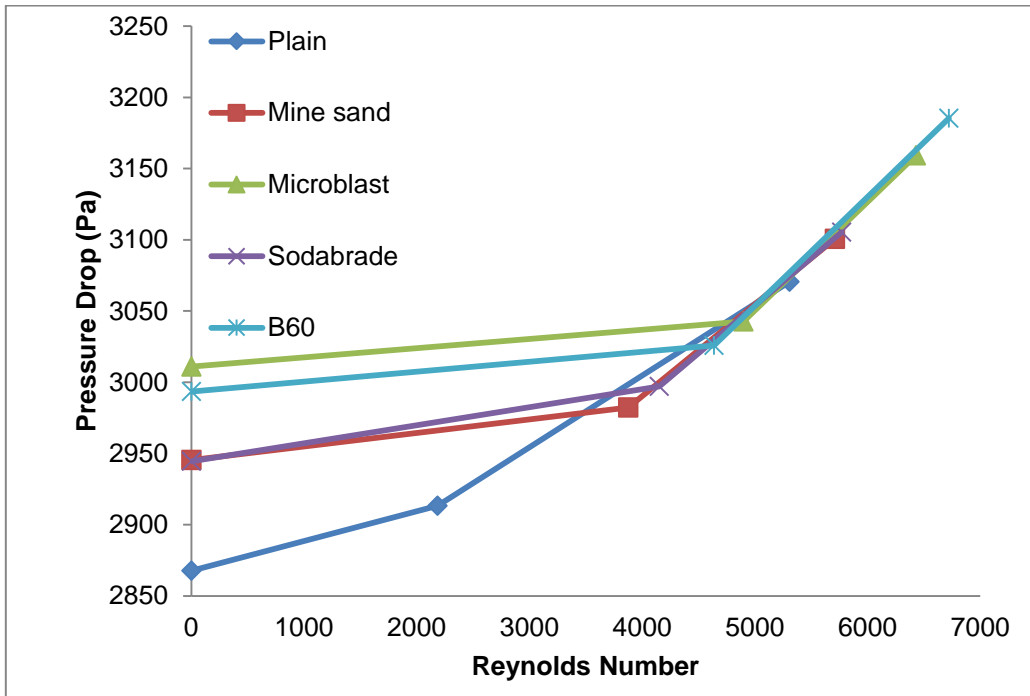
Figure 29 Pressure drop vs Reynolds number
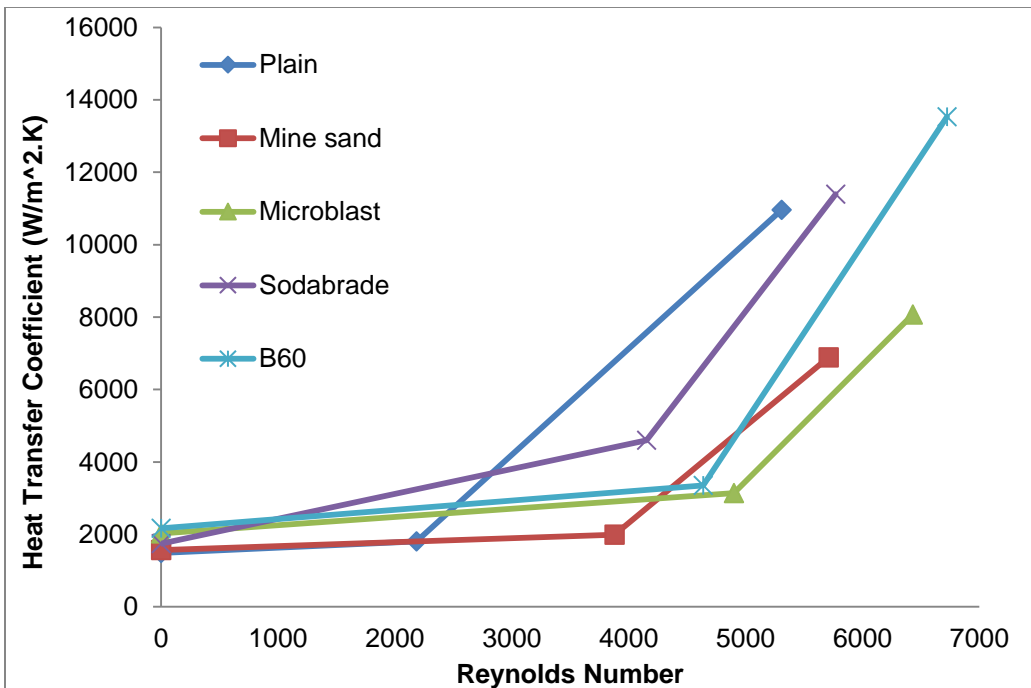
Figure 30 Heat transfer coefficient vs Reynolds number

5 Analysis of results

5.1 Introduction

From the results, it can be seen that some in-depth understanding was required to explain what really happened in the test section. The inner-glass velocities were calculated from the energy equation. This related the heat transfer coefficient with a velocity inside the glass and enabled the calculation of the Reynolds number and friction factor.

5.2 Optimisation
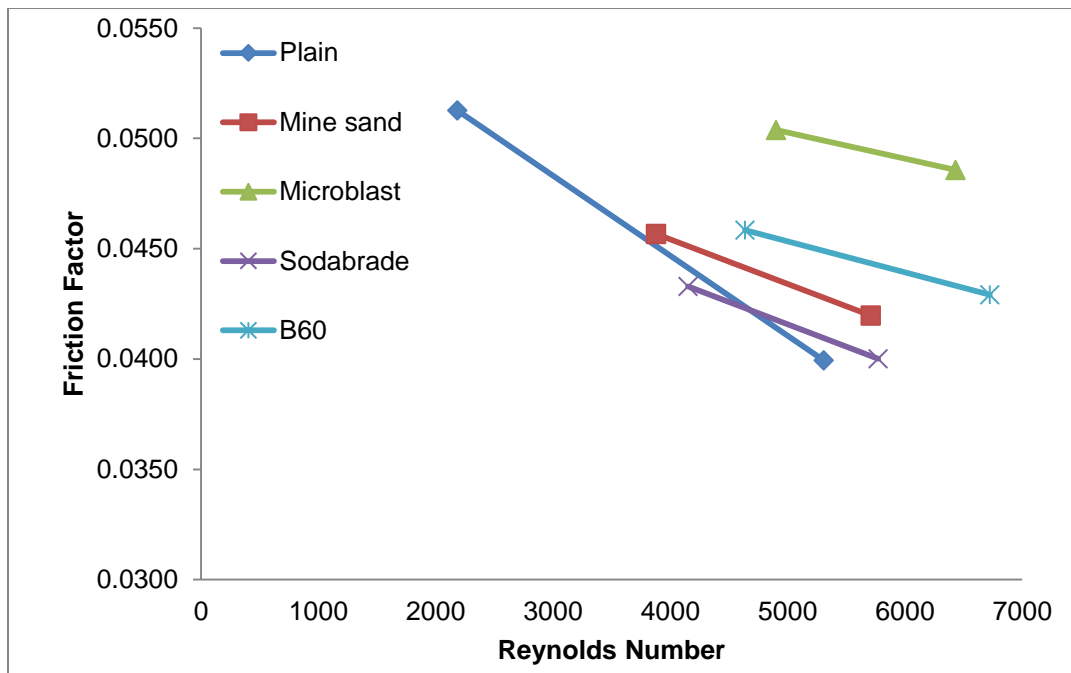
Figure 31 Friction factor vs Reynolds number

In **Figure 31** the friction factors are shown. At first glance it does not make much sense especially with the one point from the Plain rod having the highest friction factor than the rest. The roughest rods B60 and Microblast are in the middle of the data group. The relative roughnesses are close on the Moody chart resulting in a small difference in friction factor. The difference in relative roughness in this case is not large enough to offset the effect the Reynolds has on the friction which creates an inversely proportional relationship.
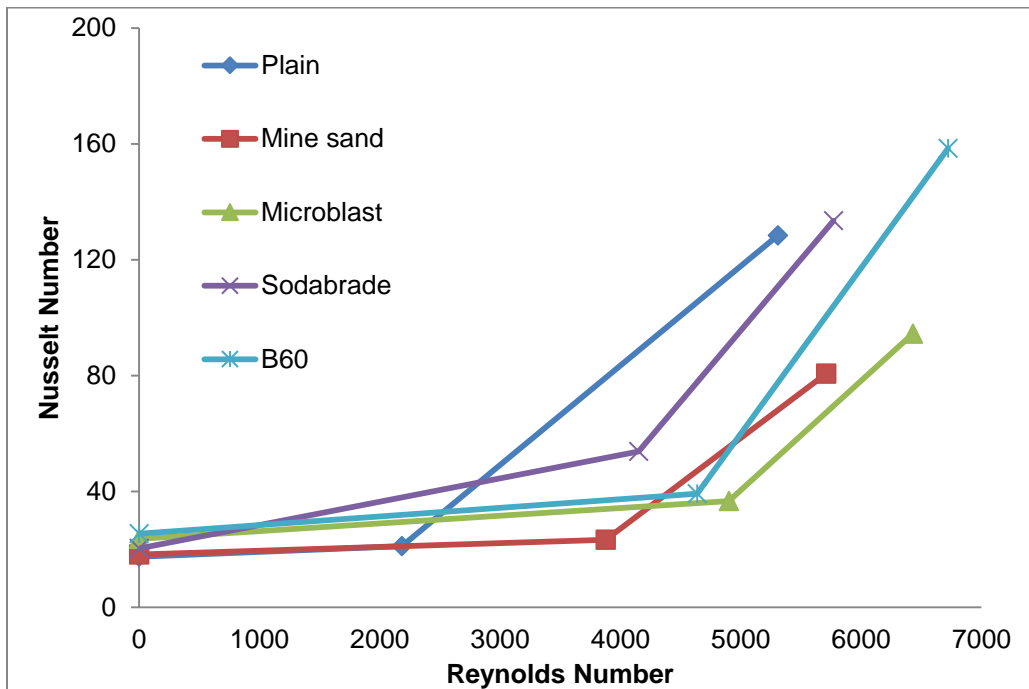
Figure 32 Nusselt number vs Reynolds number

As can be seen in **Figure 32, Figure 33** and **Figure 34**, the Sodabrade® and B60 rods demonstrated overall improved heat transfer. This does not simply imply the roughness of B60 should be used in industry, as this roughened rod will increase the pumping power needed, which translates into higher operating costs. Considering the bandwidth of uncertainty; it is unclear whether Sodabrade or B60 has the outright highest heat transfer coefficient and could possibly be virtually the same as the plain rod. These factors suggest that continuing with the plain rod would be the best option as there is little evidence any of the roughened rods absolutely improve heat transfer without any considerable pressure drop drawback. It is also noted that the heat transfer starkly increases at an approximate Reynolds numbers of 4000. This correlates well with the transition from laminar to turbulent flow.
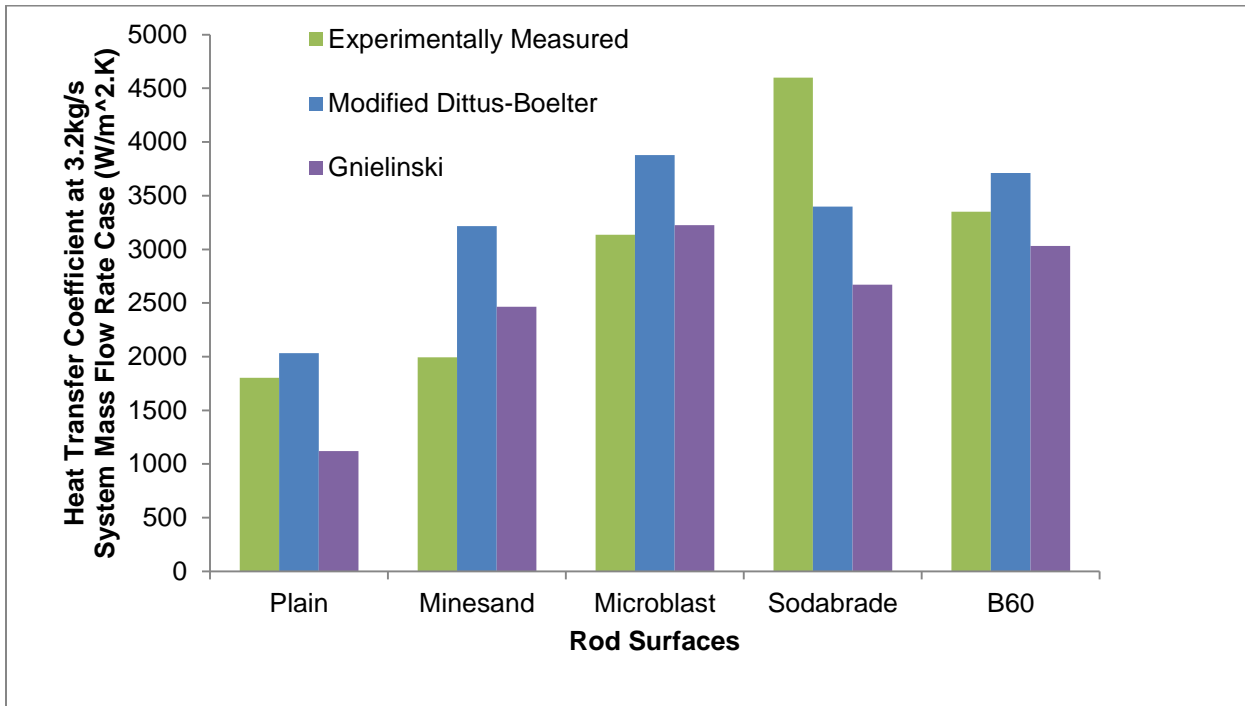
Figure 33 Heat transfer coefficient correlations at 3.2kg/s vs rod surfaces
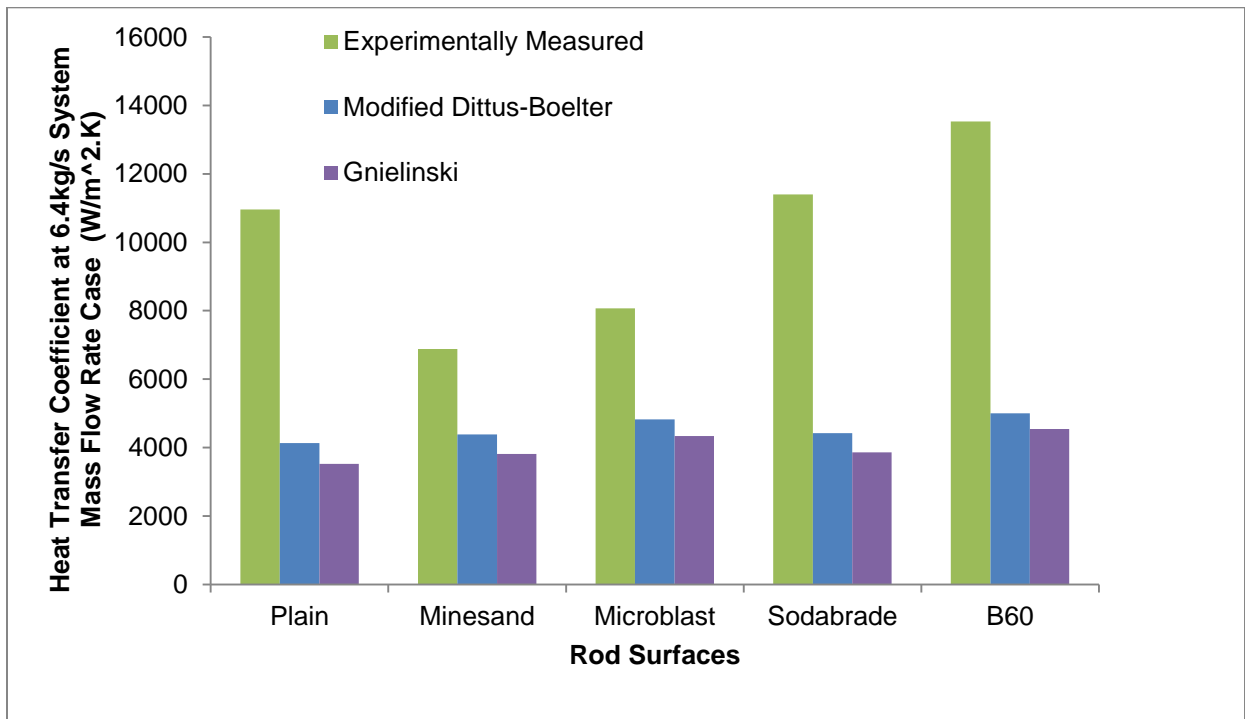
Figure 34 Heat transfer coefficient correlations at 6.4kg/s vs rod surfaces

56

The heat transfer coefficients were compared with two other commonly used relations relevant to heat transfer at hand namely the Gnielinski and modified Dittus Boelter correlations [4].

An average deviation of 16.49% separated the relations for the 3.2kg/s system mass flow rate case and an average deviation of 52.63% separated the relations for the 6.4kg/s system mass flow rate case. In conclusion, the measured heat transfer coefficients correlated well with the equations in literature for the 3.2kg/s but differed significantly for the 6.4kg/s case. This can be due to a variety of reasons with the most likely being the erratic nature of the results the faster the fluid went.
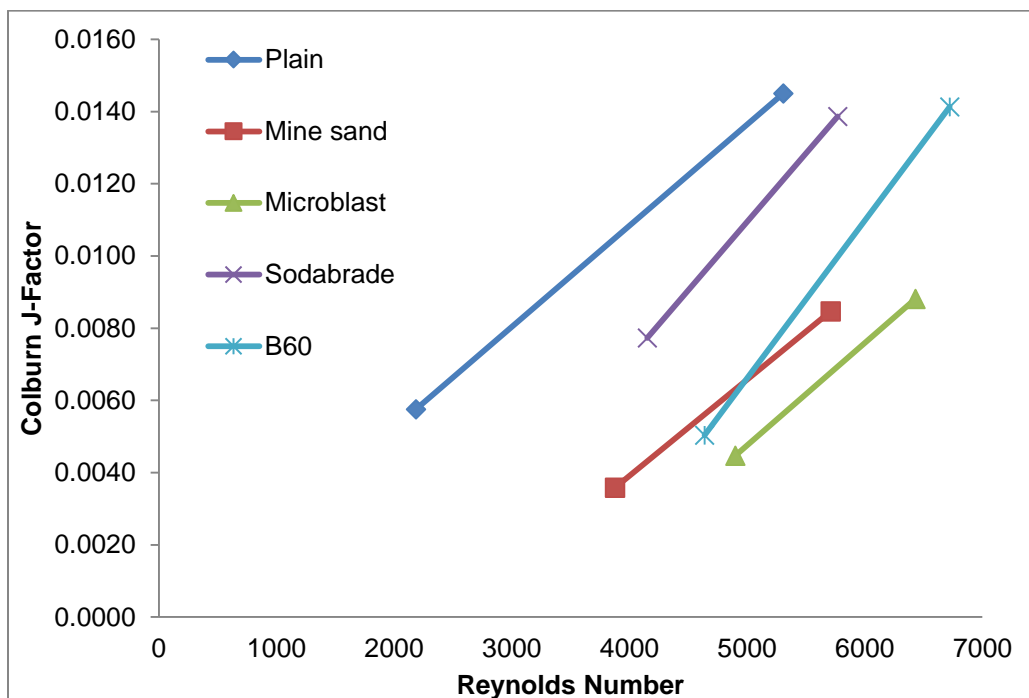
Figure 35 Heat transfer coefficient correlations at 3.2kg/s vs rod surfaces

In **Figure 35** the Colburn J-factor was calculated for both system mass flow rates and it was noted they increased with an increase in Reynolds number.

$$j = \frac{Nu}{RePr^{\left(\frac{1}{3}\right)}} \qquad (338)$$

The Colburn J-factor is effective in normalising the test results. It can also be seen that the Plain rod, which has the smoothest surface, has the highest Colburn J-factor with the roughest rod having the lowest. This adds to the argument of the Plain rod providing the best overall heat transfer and pressure drop characteristics.

57

6 Conclusion

6.1 Conclusions

It was decided to calculate the glass enclosure velocities from the measured pressure drop using the energy equation. Velocity validation tests were performed with flow concentrators which yielded a bandwidth of velocities. The calculated velocities fell within the bandwidth of velocities.

In the end, only the onset of nucleate boiling was assumed to have been produced and formal analysis of boiling heat transfer was not done. Surface temperature measurement was investigated in this research. It was concluded that the thermocouple had to be placed underneath the surface to read the most accurate results.

The results communicated a situation on the surface where the surface temperatures were lower than the saturation temperature, in this case approximately 112 ℃. This resulted in a negative $\Delta T_{boiling}$. The surface temperatures, which can be seen in **Appendix E**, were lower than expected and meant what was happening was not on the boiling curve at all. This raised the question: what was really being observed? Was the temperature measurement incorrect or was another phenomenon happening? As discussed in **Section 2.1.10**, there are many factors that affect a boiling curve including the dissolved air in the water and the heat transfer surface. Were the bubbles being formed genuine bubbles or were they trapped air making their way through the loop? The deaeration process mentioned was standard procedure when getting rid of excess air in a system, but unfortunately, the system was not completely closed and the filter and plenum boxes only assisted in mixing up the water. This is an aspect that can be improved upon. What was taken into account was the duration of the deaeration process, which was carefully done to ensure as much air was removed. The second repetition always had less bubbles and therefore, all was done to ensure an isolated system. Even though the surface temperatures were not high enough to draw an explicit boiling curve, it was suspected that the incipience of nucleate boiling was reached.

The plain rod was chosen to be the best option. This was no surprise as the plain relatively smooth rod has been used in industry for roughly 50 years now [2]. This conclusion relates well to what is standard practice in modern industry. Ultimately these tests show that roughness does not play a major role in improving the heat transfer and may well be detrimental in the performance of the cooling system since the pumping power will undoubtedly be increased.

58

Further investigation is needed to determine the erratic jumps experienced in the 6.4kg/s system mass flow rate case.

6.2 Recommendations for future work

The flow loop used in this research was designed, built and supplied for a variety of nuclear-related research topics. The undertaking was complex to start with but was completed. The flow loop was a first-generation flow loop. Keeping in mind what can better answer the question of heat transfer versus pressure drop improvements on the flow loop can be done. Some suggestions are listed below:

- Finer filters can be installed throughout the loop to minimise contaminants. Even though the water tested was of good quality, it was very easy for small cut-offs from the test section to fall into the loop. Once the debris was in the loop, it was difficult to extract it. The filter removal system can be simplified in order to facilitate the quick removal of the debris. At times, small pieces of gasket maker and other debris were spotted flowing past the test section. This was not expected to drastically affect the results but all had to be done to keep the water as pure as possible.

- Thermal insulation around the flow loop can be improved. Armaflex was cut to size and placed all over the stainless steel sections of the flow loop and this helped a lot in keeping the temperature of the set-up as constant as possible, but it is simply not good enough. This placed a limitation on the heater performance to rapidly heat up the bulk water and ultimately, rendered the heat input inadequate for future studies.

- More preheaters can be used in the flow loop to more effectively heat up the bulk water.

- New cartridge heaters are necessary to ensure uniform heat distribution because the one used in this research was very erratic in its performance. Validation tests showed that the three coils used did not perform in the same way when compared and this yielded an uneven heating profile. The heater used was significantly improved upon the first heater used, which was supplied from Germany, but it was still not up to acceptable standard. The 2300W rated heater was also not powerful enough. The power density used was advised to the author by Swift but another means is necessary to ensure easier boiling results.

- The power supply configuration must be investigated thoroughly and redesigned in order to provide more steady and reliable results. The relay and autotransformer used was most certainly not the best option for controlling the power input. The large standard

59

deviation of both the voltage and current readings points to a more profound problem. This needs to be investigated in great detail.

- An updated DAQ system must be used to measure results. The Agilent system used for these experiments experienced periods of time when the DAQ would just halt and refrain from measuring anything. This lasted a few minutes and could only be fixed by waiting.

- Thinner thermocouples can be used to more easily place them in-between the test specimen and the cartridge heater. Thinner thermocouples are a necessity if one wants to combat the EMF effect by shielding the thermocouples. The EMF effect throws in many uncertainties and therefore, the thermocouples must be shielded in order to remove the induction noise in the measurements.

- A larger test section can replace the present test section area to accommodate larger and more complicated test set-ups. This will also provide more space to improve the wiring placement, which can be very laborious in nature and which in the end equates to lost time that could have been better used in analysing the results.

- Longer windows in the test section will provide more visual feedback. An addition to visual analysis could be the purchase of a modern camera that incorporates accurate thermal imaging along with high shutter speeds in order to document bubble formation in an in-depth way.

- If the system is closed off to the environment, the deaeration process is more effective and accurate boiling curves can be achieved. Air in the system has the potential to add doubt in the investigator's mind as to what is really being observed. To remove this component can greatly benefit all future studies on the flow loop.

All of these suggestions can contribute to a more accurate system and ultimately provide answers with lower certainties. Future work suggestions include adding more rods in the test section in order to investigate the nature of heat transfer in a rod bundle array as well as implementing all the listed suggestions.

7 References

[1] J. R. Lamarsh and A. J. Baratta, *Introduction to nuclear engineering 3rd edition*. Upper Saddle River, NJ: Prentice-Hall, 2012.

[2] A. W. Chang, "Reactor grade zirconium alloys for nuclear waste disposal." Allegheny Technologies, Pittsburgh, PA, 2003.

[3] C. Govinder, "Theoretical analyses and the design, construction and testing of a flow loop for the study of generalized forced and natural convection boiling heat transfer phenomena on typical light water reactor fuel pin configurations," . University of Pretoria, 2016.

[4] Y. Cengel, *Heat and mass transfer 3rd edition*. New York, NY: McGraw-Hill, 2006.

[5] F. White, *Fluid mechanics 6th edition*. New York: McGraw-Hill, 2008.

[6] L. Cheng and T. Chen, "Comparison of six typical correlations for upward flow boiling heat transfer with kerosene in a vertical smooth tube," *Heat Transf. Eng.*, vol. 21, no. 5, 2000.

[7] K. Kok, *Nuclear engineering handbook*. Boca Raton, FL: CRC Press, 2009.

[8] V. Bessiron, "Modelling of clad-to-coolant heat transfer for RIA," *J. Nucl. Sci. Technol.*, vol. 44, no. 2, pp. 211–221, 2007.

[9] S. Nukiyama, "The maximum and minimum values of the heat Q transmitted from metal to boiling water under atmospheric pressure," *Int. J. Heat Mass Transf.*, vol. 9, pp. 1419–1433, 1966.

[10] K. J. Bell and A. C. Mueller, "Boiling heat transfer on external surfaces," *Wolver. Tube Heat Transf. Data B.*, pp. 1–38, 2006.

[11] L. Zou, "Experimental study on subcooled flow boiling on heating," 2010.

[12] L. S. Tong, "Heat transfer mechanisms in nucleate and film boiling," *Westinghouse Electr. Corp.*, 1971.

[13] S. Kandlikar, "Bubble nucleation, growth and departure in flow boiling." .

[14]   S. G. Kandlikar and M. E. Steinke, "Single-phase flow characteristics and effect of dissolved gases on heat transfer near saturation conditions in microchannels," in *ASME International Mechanical Engineering Congress and Exposition*, 2002.

[15]   T. Vorburger and J. Raja, "Surface finish metrology tutorial," Gaithersburg, 1990.

[16]   P. Blau, R. Martin, and L. Riester, "A comparison of several surface finish measurement methods as applied to ground ceramic and metal surfaces," *Oak Ridge Natl. Lab.*, no. ORNL/M-4924, 1996.

[17]   B. J. Jones, J. P. McHale, and S. V. Garimella, "The influence of surface roughness on nucleate pool boiling heat transfer," *Birck NCN Publ.*, 2009.

[18]   M. Kang, "Effect of surface roughness on pool boiling heat transfer," *Int. J. Heat Mass Transf.*, vol. 43, pp. 4073–4085, 2000.

[19]   "Introduction To thermocouples," *Dataforth Corp.*

[20]   "Thermocouple theory," *Pyromation inc.*

[21]   C. J. Kobus, "True fluid temperature reconstruction compensating for conduction error in the temperature measurement of steady fluid flows," *Rev. Sci. Instrum.*, vol. 77, 2006.

[22]   Endress+Hauser, "Calibration certificate differential pressure transducer." 2014.

[23]   "Gero Engineering." [Online]. Available: http://www.sa-business-directory.co.za/business/gero-engineering.

[24]   "Storm 100lt blast pot." [Online]. Available: http://www.stormmachinery.co.za/product/abrasive-air-blasting/storm-blast-pots/storm-100lt-blast-pot.

[25]   W. Grote, "XRD mine sand." 2013.

[26]   "Blastrite technical product information." 2009.

[27]   BAMR, "Elcometer 124 thickness gauge." BAMR, Claremeont.

[28]   WIKA, "Thermocouple specifications." .

[29]   C. Popiel and J. Wojtkowiak, "Simple formulas for thermophysical properties of liquid water for heat transfer calculations (from 0C to 150C)," *Heat Transf. Eng.*, no. 19, pp. 87–101, 1998.

[30]   Agilent Technologies, "Making good thermocouples measurements in noisy environments." 2008.

[31]   International Atomic Energy Agency (IAEA), "Thermophysical properties database of materials for light water reactors and heavy water reactors," Vienna: IAEA, 2006.

[32]   R. J. Moffat, "Describing the uncertainties in experimental results," *Exp. Therm. Fluid Sci.*, no. 1, pp. 3–17, 1988.

[33]   M. Everts, "Heat transfer and pressure drop of developing flow in smooth tubes in the transitional flow regime," University of Pretoria, 2014.

[34]   JCGM, "Evaluation of measurement data-guide to the expression of uncertainty in measurement." 2008.

[35]   WIKA, "Wika operating instructions pressure transmitter model A-10." .

[36]   ETI, "Electronic temperature instruments Ltd." 2010.

[37]   PolyScience, "Polyscience circulating baths." .

[38]   UT, "Digital clamp meters UT202A." .

APPENDIX A: WATER PROPERTIES

The water properties were calculated using the research done by Popiel and Wojtkowiak [29]. This was done in order to accurately calculate the properties without having to input large matrices of tables, which would have required processing power to retrieve the appropriate values. The equations were valid for water between $0\,°C$ and $150\,°C$. The properties were calculated using the mean bulk fluid temperature of the test section. **Equations A.1 to A.5** were calculated using the coefficients found in **Table A.1**.

$$\rho = c_0 + c_1 T + c_2 T^2 + c_3 T^{2.5} + c_4 T^3 \tag{A.1}$$

$$C_p = c_0 + c_1 T + c_2 T^{1.5} + c_3 T^2 + c_4 T^{2.5} \tag{A.2}$$

$$k = c_0 + c_1 T + c_2 T^{1.5} + c_3 T^2 + c_4 T^{0.5} \tag{A.3}$$

$$\mu = \frac{1}{c_0 + c_1 T + c_2 T^2 + c_3 T^3} \tag{A.4}$$

$$Pr = \frac{1}{c_0 + c_1 T + c_2 T^2 + c_3 T^3} \tag{A.5}$$

Table A: Water property coefficients

Constants	ρ	C_p	k	μ	Pr
c_0	999.79684	4.2174356	0.5650285	557.82468	0.074763403
c_1	0.068317355	-0.005618162	0.0026363895	19.408782	0.0029020983
c_2	-0.010740248	0.0012992528	-0.000125169	0.1360459	2.8606181E-5
c_3	0.00082140905	-0.000115353	-1.515491E-6	-3.11608E-4	-8.139553E-8
c_4	-2.3030988E-5	4.14964E-6	-0.000941294	-	-

APPENDIX B: BASELINE PARAMETERS AND TESTS
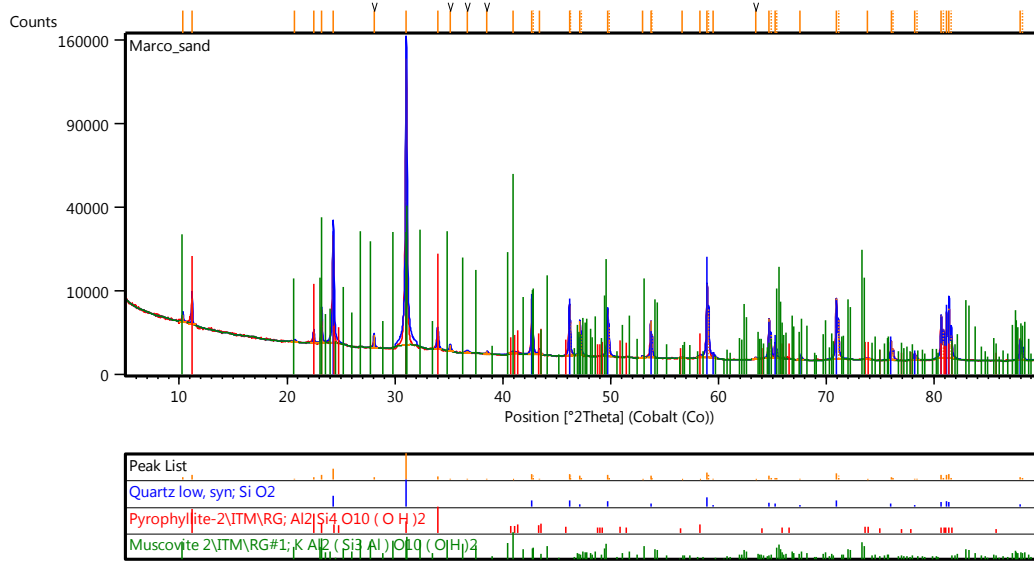
Figure B: XRD results
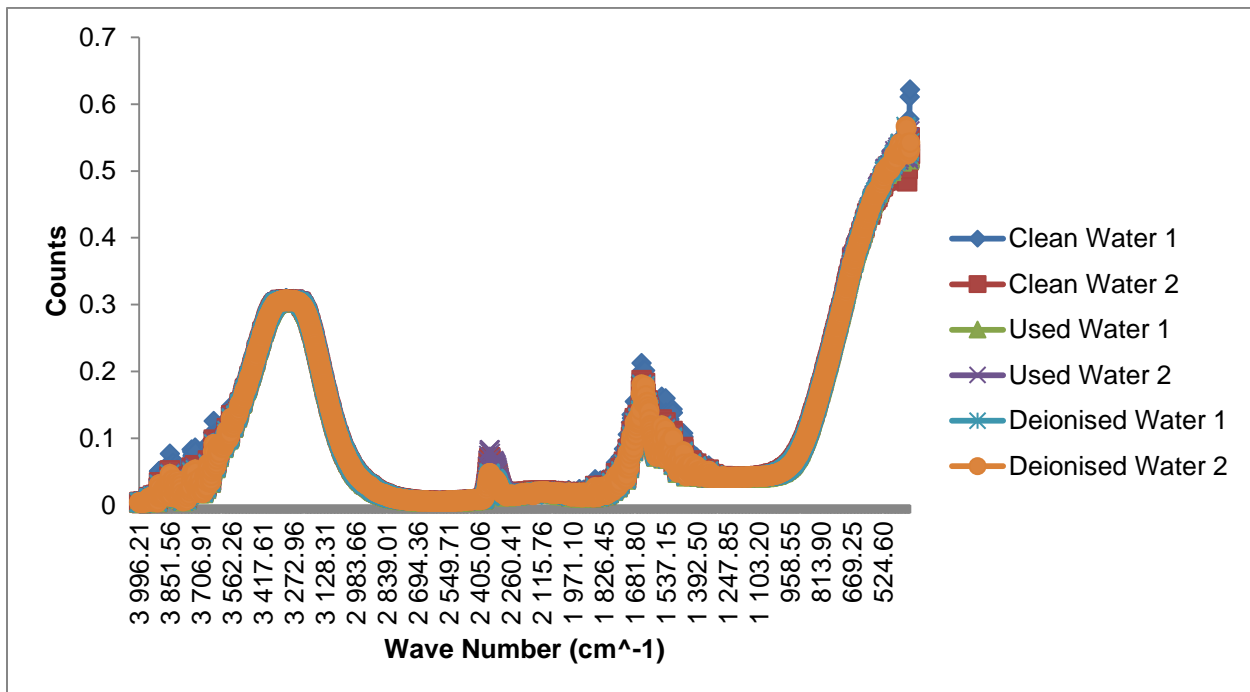
Figure B: Spectroscopic infrared scans on various types of water

APPENDIX C: FLOW CONCENTRATORS
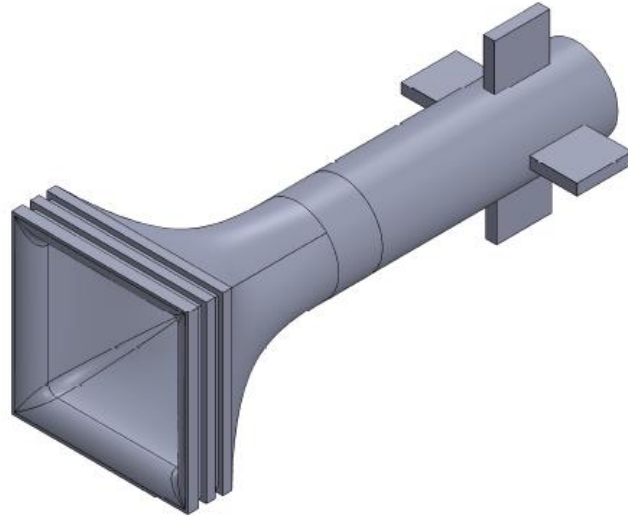
Figure C: Inlet Flow Concentrator
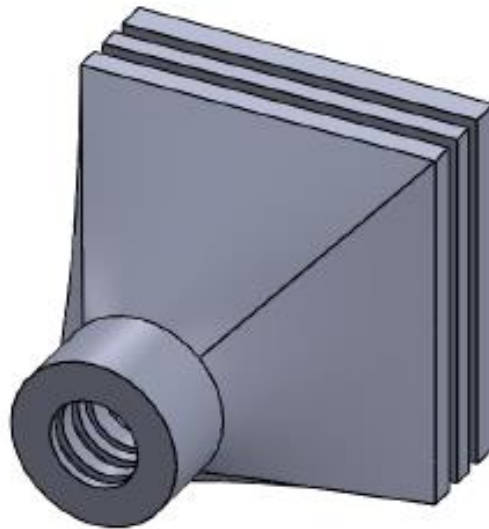
Figure C: Outlet Flow Concentrator

APPENDIX D: CALIBRATIONS AND VALIDATIONS

Table D: Pressure transducer calibration curves

Pressure transducer	m	c
Test section inlet	0.2499	-0.002
Test section outlet	0.2502	-0.0041
Total pressure inner-glass bulk fluid	0.2501	-0.0029

Table D: PT100 and thermocouple calibration curves

PT 100 and thermocouples	m	c
PT 100	0.9979	-0.1676
TC 2 long embedded	1.0012	-0.0184
TC 4 middle embedded	1.0046	0.1611
TC 5 short embedded	0.9982	0.4582
Test section inlet bulk fluid	1.0031	-0.2525
Test section outlet bulk fluid	1.005	-0.5789
TC 3 inner-glass bulk fluid	1.0017	0.1807

Table D: DP and venturi calibration curves

Mass flow meter	m	c
Venturi and DP	6.6079	-4.0808

Table D: Power calibration curves

Power	m	c
Voltage	1.0294	0.1746
Current	1.6119	0.8879

Table D: Pressure validation at 1 atmosphere (87.5 kPa)

	Rho (kg/m^3)	g (m^2/s)	h (m)	Pressure (kPa)	Error calculated (%)
Pressure outlet calculated	997	9.81	1.5	102.170855	
Pressure inlet calculated	997	9.81	2.5	111.951425	
Pressure outlet measured				100.48	-1.65
Pressure inlet measured				110.62	-1.19
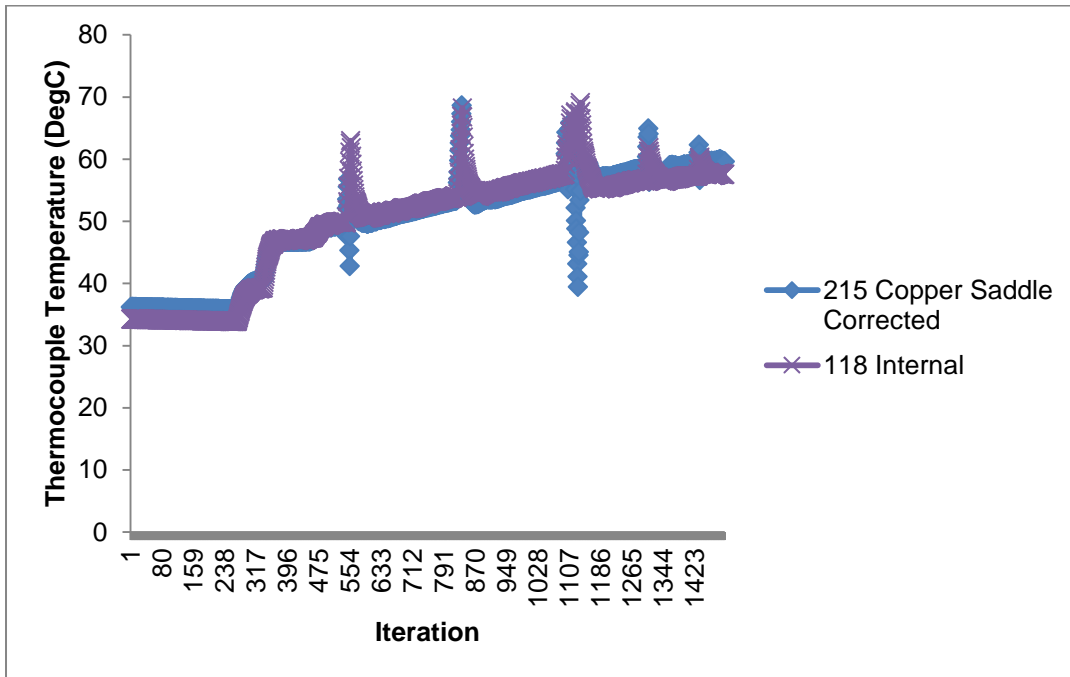
Figure D: Copper saddle vs internal thermocouple
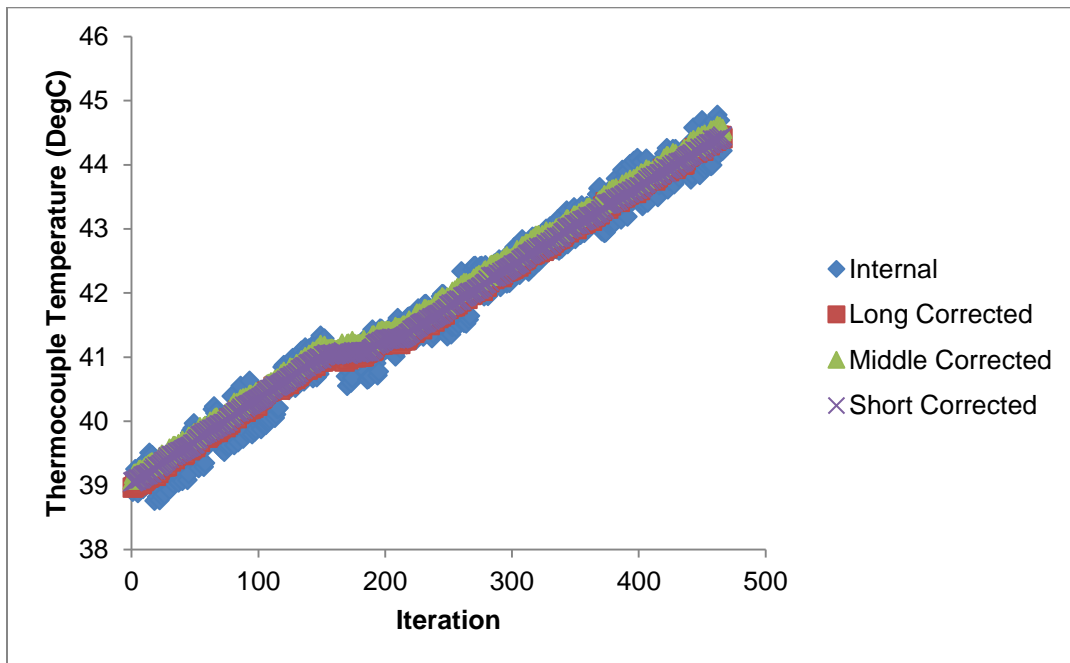
Figure D: Immersion heater thermocouple temperatures
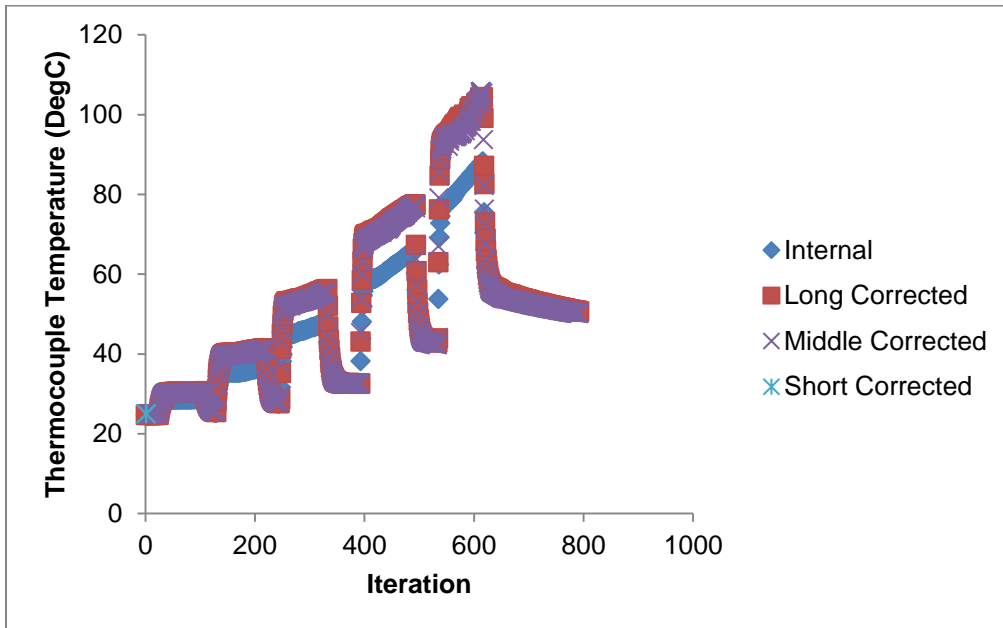
Figure D: Mock tank pool boiling thermocouple temperatures

y = 0.1482x - 4.9702
y = 0.1427x - 4.717
y = 0.1371x - 4.4638
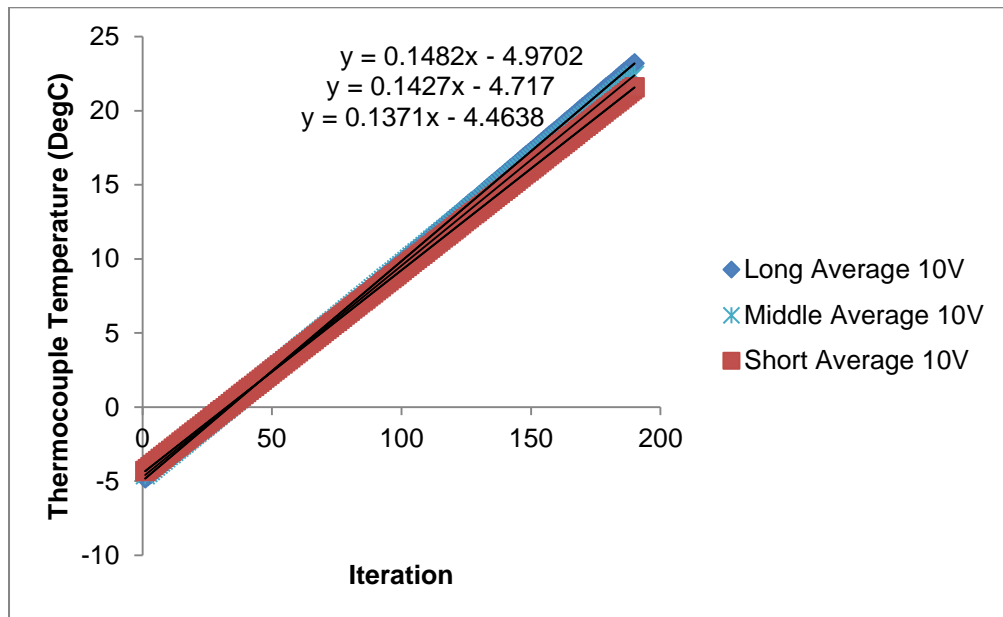
Figure D: EMF corrections

Table D: EMF correction curves

EMF corrections	M	c
Long TC2 embedded	0.1482	-4.9702
Middle TC4 embedded	0.1427	-4.717
Short TC5 embedded	0.1371	-4.4638

D3

APPENDIX E: TEST RESULTS

Plain

0kg/s

	T/S In P/T (Bar)	T/S Out P/T (Bar)	DeltaP (Bar)	3.2kg/s
Rep1	1.534121569	1.505396078	0.02872549	Rep1
Rep2	1.541364943	1.512816092	0.028548851	Rep2
Rep3	1.51599182	1.482791411	0.028807771	Rep3
Rep4	1.530915572	1.502178236	0.028737336	Rep4
Rep5	1.53358163	1.504864796	0.028716837	Rep5
Rep6	1.545448421	1.51688	0.028568421	Rep6
Average:			0.028675843	Average:

2867.584303 Pa

3.2kg/s

	T/S In P/T (Bar)	T/S Out P/T (Bar)	DeltaP (Bar)	6.4kg/s
Rep1	1.541859	1.512897698	0.028961637	Rep1
Rep2	1.526565	1.497383523	0.029181818	Rep2
Rep3	1.540096	1.511096419	0.029	Rep3
Rep4	1.520819	1.491775168	0.029043624	Rep4
Rep5	1.527819	1.498649412	0.029169412	Rep5
Rep6	1.517888	1.488620137	0.029267735	Rep6
Average:			0.029132518	Average:

DeltaPflow (Bar) 0.000456675
45.66747007 Pa

6.4kg/s

	T/S In P/T (Bar)	T/S Out P/T (Bar)	DeltaP (Bar)
Rep1	1.511146341	1.480479675	0.03067
Rep2	1.548709135	1.518173077	0.03054
Rep3	1.529926893	1.499498695	0.03043
Rep4	1.535359331	1.50478273	0.03058
Rep5	1.5404321	1.509066667	0.03108
Rep6	1.533382653	1.502466837	0.03092
Average:			0.03071

DeltaPflow (Bar) 0.00203
203.080 Pa

Heat Transfer Coefficients Calculated from Averages

0kg/s

	T/S Surface (DegC)	T/S Bulk Fluid (DegC)	q/A (W/m^2)	DeltaP (Bar)	h (W/m^2.K)
Rep1 (No TC3)	98.84311508	45	98078.76697		1821.565614
Rep2 (No TC3)	100.5857966	45	91339.19566		1643.211058
Rep3 (No TC3)	113.4996494	45	91345.18222		1333.513134
Rep4 (No TC3)	136.7782027	45	119900.1891		1306.412477
Rep5 (No TC3)	102.0668974	45	96885.38511		1697.751052
Rep6 (No TC3)	115.6698171	45	103542.8709		1465.163985
Average:	113.7200726	45	100602.5646		1489.210341

3.2kg/s

	T/S Surface (DegC)	T/S Bulk Fluid (DegC)	q/A (W/m^2)	DeltaP (Bar)	h (W/m^2.K)
Rep1 (No TC3)	79.65495964	37	93478.84856	0.02896	2191.511828
Rep2 (No TC3)	101.8292196	37	112680.8933	0.02919	1738.118921
Rep3 (No TC3)	102.4216892	37	111095.2149	0.02900	1698.14042
Rep4 (No TC3)	98.51477717	37	111624.8941	0.02903	1814.602917
Rep5 (No TC3)	82.12585591	37	86768.50371	0.02917	1922.811257
Rep6 (No TC3)	99.37125536	37	114736.352	0.02926	1839.57099
Average:	96.85255946	37	107381.1716	0.02913	1802.648901

6.4kg/s

	T/S Surface (DegC)	T/S Bulk Fluid (DegC)	q/A (W/m^2)	DeltaP (Bar)	h (W/m^2.K)
Rep1 (No TC3)	41.87345244	36.5	98375.76208	0.0307	18307.7385
Rep2 (No TC3)	41.6754524	36.5	105346.6253	0.0305	20355.05635
Rep3 (No TC3)	45.87816916	36.5	116153.3835	0.0304	12385.5074
Rep4 (No TC3)	51.97436018	36.5	104253.5535	0.0306	6737.180234
Rep5 (No TC3)	49.42873756	36.5	100105.312	0.0311	7742.852812
Rep6 (No TC3)	48.38452196	36.5	90254.64687	0.0309	7594.301831
Average:	47.46824825	36.5	103222.7042	0.0307	10962.97972

Bulk Fluid Temps Assumed Averages from Microblast, Sodabrade, B60
Based on Average Test Section Temperatures Bulk Fluid Properties

	Pr	k	Mhu	Rho
0kg/s	4.536421547	0.615604828	0.001	992.9064323
3.2kg/s	4.9316928	0.6120656	0.001	994.3150171
6.4kg/s	4.895863427	0.61223376	0.001	994.2356844
Average:	4.787992591	0.613301396	0.001	993.8190446

Figure E: Plain rod heating results

Minesand

0kg/s	T/S In P/T (Bar)	T/S Out P/T (Bar)	DeltaP (Bar)	3.2kg/s	T/S In P/T (Bar)	T/S Out P/T (Bar)	DeltaP (Bar)	6.4kg/s	T/S In P/T (Bar)	T/S Out P/T (Bar)	DeltaP (Bar)
Rep1	1.53102381	1.501821429	0.029202381	Rep1	1.535220	1.505608586	0.029611111	Rep1	1.536455587	1.505088825	0.03137
Rep2	1.529689751	1.500238227	0.029451524	Rep2	1.530296	1.500478114	0.029818182	Rep2	1.526114754	1.495456284	0.03066
Rep3	1.524072785	1.494515823	0.029556962	Rep3	1.518834	1.489158809	0.029674938	Rep3	1.55164	1.504775	0.03116
Rep4	1.522388889	1.492953216	0.029435673	Rep4	1.519703	1.488920879	0.029782418	Rep4	1.517241573	1.486047753	0.03119
Rep5	1.520557276	1.491213622	0.029343653	Rep5	1.530164	1.500263636	0.0299	Rep5	1.541240896	1.510442577	0.03080
Rep6	1.523004246	1.49352017	0.029484076	Rep6	1.534214	1.504272464	0.029942029	Rep6	1.529387716	1.498172745	0.03121
Average:			0.029454378 Average:				0.029823513 Average:				0.00155
			2945.437755 Pa				36.91357164 Pa				155.124 Pa

DeltaPflow (Bar) 0.000369136

DeltaPflow (Bar)

Heat Transfer Coefficients Calculated from Averages

Bulk Fluid Temps Assumed Averages from Microblast, Sodabrade, B60

0kg/s	T/S Surface (DegC)	T/S Bulk Fluid (DegC)	q/A (W/m^2)	h (W/m^2.K)	3.2kg/s	T/S Surface (DegC)	T/S Bulk Fluid (DegC)	q/A (W/m^2)	h (W/m^2.K)	6.4kg/s	T/S Surface (DegC)	T/S Bulk Fluid (DegC)	q/A (W/m^2)	h (W/m^2.K)	DeltaP (Bar)
Rep1 (No TC3)	131.9813003	45	83279.30309	957.4391596	Rep1 (No TC3)	58.6901428	37	92009.05318	4241.975446	Rep1 (No TC3)	50.2477648	36.5	108913.08	7922.239113	0.0314
Rep2 (No TC3)	109.5353404	45	92112.24991	1427.314854	Rep2 (No TC3)	73.51557655	37	89329.21112	2446.331663	Rep2 (No TC3)	51.6516785	36.5	103682.2724	6842.974561	0.0307
Rep3 (No TC3)	103.2104283	45	89149.97663	1531.512122	Rep3 (No TC3)	90.39879871	37	106249.3849	1989.733616	Rep3 (No TC3)	55.18692951	36.5	98438.00144	5267.746175	0.0312
Rep4 (No TC3)	110.4635017	45	97538.09427	1489.961455	Rep4 (No TC3)	99.61318286	37	110323.3118	1761.982169	Rep4 (No TC3)	51.76511642	36.5	114650.1142	7510.595467	0.0312
Rep5 (No TC3)	106.007388	45	102312.5719	1677.052161	Rep5 (No TC3)	85.19170116	37	96492.03428	2002.254163	Rep5 (No TC3)	50.82809658	36.5	107974.2054	7535.837355	0.0308
Rep6 (No TC3)	107.2397751	45	108547.0048	1689.71645	Rep6 (No TC3)	98.95947857	37	109634.7924	1769.459572	Rep6 (No TC3)	51.4207568	36.5	108507.9347	7272.280898	0.0312
Average:	107.6912867	45	97931.97949	1563.111408	Average:	89.53574757	37	102405.7469	1993.952237	Average:	52.1705073	36.5	106650.5056	6885.886891	0.0310

	Pr	k	Mhu	Rho
0kg/s	4.46358246	0.616334804	0.001	992.560471
3.2kg/s	4.810500546	0.613088525	0.001	993.9331809
6.4kg/s	4.7090165	0.6139915	0.001	993.587222
Average:	4.661033169	0.61447161	0.001	993.3602913

Based on Average Test Section Temperatures Bulk Fluid Properties

Figure E: Mine sand rod heating results

Microblast

0kg/s

	T/S In P/T (Bar)	T/S Out P/T (Bar)	Total Press P/T9 (Bar)	Dynamic Calculated (Bar)	DeltaP (Bar)	
Rep1	1.52189095	1.492090487	1.492911833	0.000821346	0.029800	Rep1
Rep2	1.517633603	1.48804251	1.488631579	0.000589069	0.029591	Rep2
Rep3	1.529208696	1.499107246	1.499802029	-0.00108696	0.030101	Rep3
Rep4	1.531904478	1.501653731	1.498819403	-0.00273433	0.030251	Rep4
Rep5	1.522697531	1.492570988	1.48720679	-0.0053642	0.030127	Rep5
Rep6	1.510772	1.480296	1.474616	-0.00568	0.030476	Rep6
Average:				-0.0028528	0.030109	Average:
				-285.528272	3010.917 Pa	

3.2kg/s

	T/S In P/T (Bar)	T/S Out P/T (Bar)	Total Press P/T9 (Bar)	Dynamic Calculated (Bar)	DeltaP (Bar)	
	1.512314667	1.482261333	1.478256	-0.00400533	0.03005	Rep1
	1.503670194	1.473560847	1.473978836	0.000417989	0.03011	Rep2
	1.502376307	1.471728223	1.473407666	0.001679443	0.03065	Rep3
	1.52540625	1.49483125	1.49271875	-0.0021125	0.03057	Rep4
	1.501091255	1.470676806	1.462745247	-0.00793156	0.03041	Rep5
	1.517814346	1.48742616	1.483181435	-0.00424473	0.03039	Rep6
				-0.00243827	0.03043	Average:
			DeltaPflow (Bar)	-243.827055	31.78467 Pa	

6.4kg/s

	T/S In P/T (Bar)	T/S Out P/T (Bar)	Total Press P/T9 (Bar)	Dynamic Calculated (Bar)	DeltaP (Bar)	
	1.496864078	1.465889968	1.466902913	0.001012945	0.0310	Rep1
	1.50910796	1.47758982	1.477997006	0.000407186	0.0315	Rep2
	1.516745308	1.485402145	1.48191689	-0.00348525	0.0313	Rep3
	1.50075319	1.468968085	1.4705	0.001531915	0.0318	Rep4
	1.516804082	1.484906122	1.483665306	-0.00124082	0.0319	Rep5
	1.508120773	1.47669082	1.472671498	-0.0040932	0.0314	Rep6
				-0.00136126	0.0316	
			DeltaPflow (Bar)	-136.125883	148.49 Pa	

Heat Transfer Coefficients Calculated from Averages

0kg/s

	T/S Surface (DegC)	T/S Bulk Fluid (DegC)	q/A (W/m^2)	h (W/m^2.K)	DeltaP (Bar)	
Rep1 (No TC3)	107.9347519	45	103531.0589	1645.053896	0.029797	Rep1 (No TC3)
Rep2 (No TC3)	99.84410592	45	101576.5705	1852.096388	0.029590	Rep2 (No TC3)
Rep3 (TC3)	98.39069826	49.72879356	121390.8823	2494.577289	0.030112	Rep3 (TC3)
Rep4 (TC3)	98.76608915	50.42946279	104492.4544	2161.765564	0.030252	Rep4 (TC3)
Rep5 (TC3)	111.3397845	52.38709349	112031.7569	1900.367142	0.030125	Rep5 (TC3)
Rep6 (TC3)	103.2447887	49.71053107	91821.13624	1715.184637	0.030478	Rep6 (TC3)
Average:	102.3170933	49.45117618	106262.5601	2024.798204	0.030111	Average:

	Pr	k	Mhu	Rho
0kg/s	4.275794622	0.618075515	0.001	991.8369479
3.2kg/s	4.572522103	0.615260454	0.001	993.1033919
6.4kg/s	4.472443648	0.616166775	0.001	992.7546248
Average:	4.440253458	0.616500915	0.001	992.5649882

Bulk Fluid Temps Assumed Averages from Microblast, Sodabrade, B60 (Few Reps)

3.2kg/s

	T/S Surface (DegC)	T/S Bulk Fluid (DegC)	q/A (W/m^2)	h (W/m^2.K)	DeltaP (Bar)	
	67.91830774	37	110039.6961	3559.046537	0.03005	Rep1 (No TC3)
	77.67647961	37	119895.5054	2947.538887	0.03011	Rep2 (No TC3)
	75.21828015	37.83140688	107220.4984	2867.864816	0.03064	Rep3 (TC3)
	88.71845286	40.05503158	114188.5651	2346.496857	0.03058	Rep4 (TC3)
	62.62880276	41.7290927	103131.0321	4934.5676	0.0304	Rep5 (TC3)
	79.95896904	41.84289255	98512.45588	2584.538204	0.03039	Rep6 (TC3)
	76.84019688	39.69168474	108589.6114	3136.201273	0.03043	Average:

Based on Average Test Section Temperatures Bulk Fluid Properties

6.4kg/s

	T/S Surface (DegC)	T/S Bulk Fluid (DegC)	q/A (W/m^2)	h (W/m^2.K)	DeltaP (Bar)	
	46.47114805	36.5	107984.3676	10829.68251	0.0310	Rep1 (No TC3)
	49.52447956	35.73933184	105635.5181	7662.995006	0.0315	Rep2 (TC3)
	49.77453722	38.1702277	101730.278	8766.583391	0.0313	Rep3 (TC3)
	50.61468816	39.5591141	88474.05795	8002.665211	0.0318	Rep4 (TC3)
	52.67361862	40.9695447	95987.0362	8201.16456	0.0319	Rep5 (TC3)
	53.85587094	41.54832906	95003.64234	7719.140282	0.0314	Rep6 (TC3)
	51.2886389	39.1973065	97366.10651	8070.50969	0.0316	Average:

Figure E: Microblast® rod heating results

Sodabrade

0kg/s

	T/S In P/T (Bar)	T/S Out P/T (Bar)	Total Press P/T9 (Bar)	Dynamic Calculated (Bar)	DeltaP (Bar)	
Rep1	1.492288462	1.463240385	1.463538462	0.000298077	0.029048	Rep1
Rep2	1.534580153	1.505538168	1.50575954 2	0.000221374	0.029042	Rep2
Rep3	1.520143791	1.491313725	1.491493464	0.000179739	0.028830	Rep3
Rep4	1.52347907	1.493893023	1.49344186	-0.00045116	0.029586	Rep4
Rep5	1.522975207	1.49314876	1.492822314	-0.00032645	0.029826	Rep5
Rep6	1.524942387	1.495	1.494983539	-1.6461E-05	0.029942	Rep6
Average:				-7.85914E-05	0.029445	Average:
				-7.85914738	2944.539 Pa	

Heat Transfer Coefficients Calculated from Averages

0kg/s

	T/S Surface (DegC)	T/S Bulk Fluid (DegC)	q/A (W/m^2)	h (W/m^2.K)	DeltaP (Bar)	
Rep1 (TC3)	91.80970952	33.95230284	85703.1653	1481.282522	0.029051	Rep1 (TC3)
Rep2 (TC3)	101.0918453	36.95636395	104545.059	1630.065868	0.029038	Rep2 (TC3)
Rep3 (TC3)	90.34061249	38.23358298	93271.45375	1789.997523	0.028830	Rep3 (TC3)
Rep4 (TC3)	110.6584049	41.63042351	114624.3423	1660.548955	0.029584	Rep4 (TC3)
Rep5 (TC3)	86.80503815	40.12190815	90470.24027	1937.96432	0.029822	Rep5 (TC3)
Rep6 (TC3)	108.288063	42.52384081	111420.5707	1694.242962	0.029942	Rep6 (TC3)
Average:	99.43679275	39.89322388	102866.3332	1742.563926	0.029443	Average:

	Pr	k	Mhu	Rho	
0kg/s	4.531023659	0.615650631	0.001	992.931724	
3.2kg/s	4.80434877	0.613093343	0.001	993.9404609	
6.4kg/s	4.753553127	0.613557649	0.001	993.7762306	
Average:	4.69630851 9	0.614100541	0.001	993.5494718	

Based on Average Test Section Temperatures Bulk Fluid Properties

3.2kg/s

	T/S In P/T (Bar)	T/S Out P/T (Bar)	Total Press P/T9 (Bar)	Dynamic Calculated (Bar)	DeltaP (Bar)	
	1.520693069	1.491023102	1.489556766	-0.00136634	0.02967	Rep1
	1.511577061	1.481913978	1.480451613	-0.00146237	0.02966	Rep2
	1.509620795	1.479700306	1.478253823	-0.00144648	0.02992	Rep3
	1.523168919	1.492942568	1.490820946	-0.00212162	0.03023	Rep4
	1.518958549	1.488927461	1.486642487	-0.00228497	0.03003	Rep5
	1.522010453	1.491993031	1.489700348	-0.00229268	0.03002	Rep6
				-0.00192163	0.02997	Average:
DeltaPflow (Bar)					0.00053	
			-192.162548	52.63006 Pa		

3.2kg/s

	T/S Surface (DegC)	T/S Bulk Fluid (DegC)	q/A (W/m^2)	h (W/m^2.K)	DeltaP (Bar)	
	50.60412	31.08369777	97922.46685	5016.411312	0.02967	Rep1 (TC3)
	54.27458307	33.00339667	104131.3825	4895.419584	0.02967	Rep2 (TC3)
	55.2372332	34.40389464	103280.5236	4957.463886	0.02992	Rep3 (TC3)
	58.90920189	35.40723403	101244.717	4307.925089	0.03023	Rep4 (TC3)
	59.32032307	36.68178604	111053.2413	4905.49549	0.03004	Rep5 (TC3)
	65.49818099	37.94821014	108418.8059	3935.351019	0.03001	Rep6 (TC3)
	58.64790445	35.4889043	105625.734	4600.331014	0.02997	Average:

6.4kg/s

	T/S In P/T (Bar)	T/S Out P/T (Bar)	Total Press P/T9 (Bar)	Dynamic Calculated (Bar)	DeltaP (Bar)	
	1.526368078	1.49486645	1.495560261	0.000693811	0.0315	Rep1
	1.518477612	1.488570896	1.487914179	-0.00065672	0.0299	Rep2
	1.529423197	1.498858934	1.499291536	0.000432602	0.0306	Rep3
	1.520511194	1.48916791	1.489149254	-1.8657E-05	0.0313	Rep4
	1.516050209	1.484338912	1.485154812	0.000815126	0.0317	Rep5
	1.537416309	1.505678112	1.506712446	0.001034335	0.0317	Rep6
				0.000321338	0.0311	Average:
DeltaPflow (Bar)					0.0016	
			32.13379122	160.74 Pa		

6.4kg/s

	T/S Surface (DegC)	T/S Bulk Fluid (DegC)	q/A (W/m^2)	h (W/m^2.K)	DeltaP (Bar)	
	35.93707808	31.46261249	107662.6198	24061.55943	0.0315	Rep1 (TC3)
	39.64522504	33.20369927	109058.496	16930.53787	0.0299	Rep2 (TC3)
	46.82652894	34.90293535	115624.9321	9697.154745	0.0305	Rep3 (TC3)
	46.37011615	35.92290465	107477.6077	10287.68373	0.0314	Rep4 (TC3)
	48.72733296	37.0320396 1	119609.1946	10227.12223	0.0318	Rep5 (TC3)
	49.83850224	38.63976355	110175.3155	9838.189693	0.0317	Rep6 (TC3)
	46.28154107	35.94026849	112389.1092	11396.13765	0.0311	Average:

Figure E: Sodabrade® rod heating results

B60

0kg/s

	T/S In P/T (Bar)	T/S Out P/T (Bar)	Total Press P/T9 (Bar)	Dynamic Calculated (Bar)	DeltaP (Bar)
Rep1	1.52930769	1.496010256	1.4964	0.000389744	0.029921
Rep2	1.539172775	1.509201571	1.50604712	-0.00315445	0.029971
Rep3	1.536333333	1.506395604	1.50578546	-0.00060806	0.029938
Rep4	1.523356877	1.493453532	1.492884758	-0.00056877	0.029903
Rep5	1.535249249	1.505339339	1.50264649	-0.00269069	0.029910
Rep6	1.529584314	1.499635294	1.497745098	-0.0018902	0.029949
Average:				-0.00178243	0.029934
				-178.243377	2993.424 Pa

3.2kg/s

	T/S In P/T (Bar)	T/S Out P/T (Bar)	Total Press P/T9 (Bar)	Dynamic Calculated (Bar)	DeltaP (Bar)
Rep1	1.547053333	1.516736667	1.51317	-0.00356667	0.03032
Rep2	1.522493917	1.492284672	1.487807786	-0.00447689	0.03021
Rep3	1.52803125	1.497589844	1.495554688	-0.00203516	0.03044
Rep4	1.523485816	1.49314539	1.491163121	-0.00198227	0.03034
Rep5	1.520996403	1.490838129	1.489647482	-0.00119065	0.03016
Rep6	1.516842657	1.486695804	1.485244755	-0.00145105	0.03015
Average:				-0.0022272	0.03026
DeltaPflow (Bar)				0.00032	
				-222.720157	32.49991 Pa

6.4kg/s

	T/S In P/T (Bar)	T/S Out P/T (Bar)	Total Press P/T9 (Bar)	Dynamic Calculated (Bar)	DeltaP (Bar)
Rep1	1.51527397	1.479859589	1.47715411	-0.00270548	0.0317
Rep2	1.512077778	1.479877778	1.481066667	0.001188889	0.0322
Rep3	1.53870614	1.506890351	1.507649123	0.000758772	0.0318
Rep4	1.52944664	1.491320158	1.491833992	0.000513834	0.0316
Rep5	1.531479365	1.499209524	1.500365079	0.001155556	0.0323
Rep6	1.51834728	1.486991632	1.487711297	0.000719665	0.0314
Average:				0.000867343	0.0319
DeltaPflow (Bar)				86.73431277	191.89 Pa

Heat Transfer Coefficients Calculated From Averages

0kg/s

	T/S Surface (DegC)	T/S Bulk Fluid (DegC)	q/A (W/m^2)	h (W/m^2.K)	DeltaP (Bar)
Rep1 (TC3)	101.1960605	42.41134741	104463.5118	1777.052338	0.029918
Rep2 (TC3)	90.65474223	46.01830482	92446.09534	2071.090363	0.029975
Rep3 (TC3)	91.01058057	48.16903375	99341.35039	2318.808675	0.029940
Rep4 (TC3)	101.7669055	50.3579533	100918.2428	1963.048041	0.029903
Rep5 (TC3)	104.8241247	53.21456089	107157.5564	2076.311995	0.029909
Rep6 (TC3)	95.1702906	52.76032341	102431.6383	2415.272756	0.029944
Average:	96.68532871	50.10403524	100458.9767	2168.906366	0.029934

	Pr	k	Mhu	Rho
0kg/s	4.442763889	0.616487434	0.001	992.5696488
3.2kg/s	4.716261732	0.613970258	0.001	993.6382075
6.4kg/s	4.633262835	0.614701916	0.001	993.3572912
Average:	4.597429485	0.615053202	0.001	993.1883825

3.2kg/s

	T/S Surface (DegC)	T/S Bulk Fluid (DegC)	q/A (W/m^2)	h (W/m^2.K)	DeltaP (Bar)
Rep1 (TC3)	64.69979394	34.83387126	99954.44411	3346.772246	0.03032
Rep2 (TC3)	66.82708385	35.85567939	111031.2586	3584.960402	0.03021
Rep3 (TC3)	70.35762589	36.82036467	103747.9124	3093.511772	0.03044
Rep4 (TC3)	76.26517454	38.00034502	111553.1413	2915.291737	0.03034
Rep5 (TC3)	74.06223947	39.07668638	106745.7889	3051.139097	0.03015
Rep6 (TC3)	67.11559552	40.75944434	108254.5145	4107.371892	0.03014
Average:	70.92554385	38.10250396	108266.5231	3350.45498	0.03026

Based on Average Test Section Temperatures Bulk Fluid Properties

6.4kg/s

	T/S Surface (DegC)	T/S Bulk Fluid (DegC)	q/A (W/m^2)	h (W/m^2.K)	DeltaP (Bar)
Rep1 (TC3)	43.58815843	33.64027784	100268.7913	10079.41242	0.0317
Rep2 (TC3)	41.6092532	34.8760043	97230.50184	14440.37151	0.0322
Rep3 (TC3)	45.05085339	36.26205886	100484.3868	11433.23882	0.0319
Rep4 (TC3)	45.19208365	37.8253681	111166.9897	15090.44145	0.0317
Rep5 (TC3)	47.82946347	39.15804495	116520.6638	13437.32441	0.0323
Rep6 (TC3)	49.02539835	40.39374512	114522.1254	13267.69303	0.0314
Average:	45.74140884	37.70304427	107984.9335	13533.81385	0.0319

**Figure E: B60 rod heating results**

APPENDIX F: UNCERTAINTY ANALYSIS

F.1 INTRODUCTION

Possible errors are always present in any experiment, which makes the uncertainty analysis a vital practice in any engineering study. Moffat [32] describes an in-depth procedure detailing all the possible error calculation methods, which was used in this research. A high uncertainty was expected in these experiments due to the nature of boiling as well as being the first official tests done on the new flow loop. A 95% confidence interval was used throughout.

F.2 THEORY

Two basic types of errors exist, namely bias and precision errors. Bias errors constitute all the fixed errors in the system such as the instrumentation used and the calibrations performed on the measuring equipment. These errors do not change over time and are often obtained from the suppliers of the measuring equipment used. Precision errors relate to all the fluctuations experienced in the system and quantify how precise the measurements taken are. For a single measurement, uncertainty is calculated with the bias and precision within a root sum square:

$$\delta x_i = \left(bi^2 + p_i^2\right)^{\frac{1}{2}}$$
(F.1)

The uncertainty for a single point, but also applicable to multi-point samples, can be expressed with odds of 20 to 1 as:

$$X_i = X_i(measured) \pm \delta X_i$$
(F.2)

The final expression is a function of a number of variables:

$$R = R(X_1, X_2, X_3, \dots, X_N)$$
(F.3)

For a single point measurement, its effect can be calculated on the overall uncertainty by:

$$\delta R_{Xi} = \frac{\partial R}{\partial X_i} \delta X_i$$
(F.4)

δR_{Xi} is also referred to as the sensitivity coefficient. For many variables, the final uncertainty is calculated by using a root sum method:

$$\delta R = \left[\sum_{i=1}^{N} \left(\frac{\partial R}{\partial X_i} \delta X_i \right)^2 \right]^{\frac{1}{2}} \tag{F.5}$$

A simpler method of calculating the uncertainty in percentage form can be done as a fraction:

$$R = X_1^a X_2^b X_3^c \dots X_M^m \tag{F.6}$$

$$\frac{\delta R}{R} = \left[\left(a \frac{\delta X_1}{X_1} \right)^2 + \left(b \frac{\delta X_2}{X_2} \right)^2 + \dots + \left(m \frac{\delta X_m}{X_m} \right)^2 \right]^{\frac{1}{2}} \tag{F.7}$$

The exponent of X_i is now the sensitivity coefficient.

The thermocouples were analysed using linear regression analysis [33]. Using Dunn's method, the uncertainty result from a mathematical relation between two or more variables can be calculated [33]. The calculated variable uncertainty can be obtained with the following equation where m is added as it is a correlated term:

$$\delta y = \pm \frac{t S_{yx}}{m} \sqrt{\frac{1}{N} + \frac{1}{M} + \frac{(x_i - \bar{x})^2}{S_{xx}}} \tag{F.8}$$

The t multiplier can be looked up with the confidence interval and degrees of freedom [34].

S_{yx} is calculated with variables a and b:

$$S_{xy} = \sum_{i=1}^{N} (x_i - \bar{x})(y_i - \bar{y}) \tag{F.9}$$

$$b = \frac{S_{xy}}{S_{xx}} \tag{F.10}$$

$$a = \bar{y} - b\bar{x} \tag{F.11}$$

$$S_{yx} = \sqrt{\frac{\sum_{i=1}^{N} (y_i - y_{ci})^2}{N - 2}} \tag{F.12}$$

and S_{xx} is:

$$S_{xx} = \sum_{i=1}^{N} (x_i - \bar{x})^2 \qquad (F.13)$$

The gradient is used to relate the calculated y variable to x variable through:

$$\delta x = \frac{\delta y}{m} \qquad (F.14)$$

F.3 EQUIPMENT

F.3.1 FLOW METER

A maximum volumetric flow rate of $23 m^3/hr$ was used through the venturi and DP, which translates to a little over 6.4kg/s in the test section. For 6.4kg/s and below, the accuracy was 0.4955% [22]. At 6.4kg/s, the accuracy was therefore 0.004955m/s and at 3.2kg/s, the accuracy was 0.0024775m/s.

F.3.2 PRESSURE TRANSDUCERS

The pressure transducers came calibrated with the manufacturers specifying the accuracy. At room temperature, the accuracy was $\leq \pm 1\%$ [35]. This applied to all the pressure transducers used.

F.3.3 THERMOCOUPLES

The general bias for a T-type thermocouple is 0.5 ℃ but to improve the accuracy of such a vital instrument, some thermocouples were calibrated in a thermal bath and others were calibrated with a PT100 probe with an accuracy of 0.04℃ [36].

The test section inlet and outlet thermocouples along with the outlet inner-glass bulk fluid thermocouple were calibrated in a thermal bath by taking 15 measuring points at 39 different temperatures between 90 ℃ and 140 ℃. The model of thermal bath used was the PD20R-30-A12E, which used the performance digital 240VAC/50Hz temperature controller. The bias uncertainty of the bath was ± 0.005 ℃ [37].The set values of the thermal bath were plotted against the read values of the thermocouples. The linear graph was used to calibrate the thermocouple.

The embedded thermocouples used in the grooves of the heater were calibrated in reference to a PT100 probe by placing everything in a bath filled with hot water at approximately 77 ℃ and allowing it to cool overnight to reach ambient. The PT100 probe came with a certificate stating

values for a linear calibration graph along with a measurement uncertainty. Once the calibration was input, the accuracy of the probe was used as the bias of the thermocouples. The precision component was calculated using the equations of Dunn found above.

The uncertainty of each thermocouple was in the range of 0.01523 ℃ and 0.11098 ℃ for sample calculations at selected average temperatures. The errors were steady around these temperatures.

F.3.4   DIMENSION MEASUREMENTS

A tape measure and a vernier were used to measure all necessary dimensions. The tape measure had an accuracy of 1mm and the vernier $20\mu m$.

F.4 FLUID PROPERTIES

The fluid properties were calculated from the empirical correlations of Popiel and Wojtkowiak detailed in **Appendix A** [29]. The uncertainties are specified in **Table F.1**.

<div align="center">

Table F: Bulk fluid property uncertainties

Property	Uncertainty
ρ	$\pm 0.001\% - \pm 0.003\%$
C_p	$\pm 0.04\%$
μ	$\pm 1\%$
k	$\pm 2\%$
Pr	$\pm 2.3\%$

</div>

The bulk fluid properties were calculated from the average temperature of the inlet and outlet fluid temperatures. These properties were assumed for all heat transfer calculations.

F.5 CALCULATED RESULTS

F.5.1   SURFACE ROUGHNESS MEASUREMENT

The Elcometer 124 thickness gauge has an accuracy of 2μm and was used to measure the surface roughness [27].

F.5.2   EMF EFFECT

The EMF uncertainty analysis was made complex due to the fact that the voltage jumps recorded experienced much scatter. The temperature measurements were matched together in

the voltage jump range it was expected to be. The tests were done with the data up to the 100V mark in order to avoid the increasing heating contribution associated with higher heat inputs. The known values, in this case the y variable, were assumed to be the EMF temperature effects from the correction curves with the bias of the procedure being the voltage uncertainty. Five measuring points were taken at 10 voltage jumps used for this analysis. At 100V, the long thermocouple was $27.642\,°C$ and the short thermocouple was $25.882\,°C$. The middle thermocouple was averaged between the two, due to its erratic nature at times.

F.5.3   HEAT TRANSFER AREA

The heat transfer area uncertainty was calculated by:

$$A = \pi DL = 2\pi rL \tag{F.16}$$

$$\delta A = \left[\left(\frac{\partial A}{\partial D}\delta D\right)^2 + \left(\frac{\partial A}{\partial L}\delta L\right)^2\right]^{0.5} \tag{F.17}$$

$$\delta A = [(\pi L\delta D)^2 + (\pi D\delta L)^2]^{0.5} \tag{F.18}$$

F.5.4   HEAT INPUT

The voltage and current measurements had to be calibrated and the calibration was done by a hand-held multimeter, namely UNI-T-UT202A with an AC voltage error of 1.2% and an AC current error of 1.5%. A calibration test was used to obtain a linear calibration curve [38]. The calibration test was done with a marginally more powerful heater of 3 000W, which was acceptable because it was the measuring equipment that had to be calibrated. The final errors at max voltage and max current were 18.8528V and 0.6552A respectively.

The heat input uncertainty was calculated by considering the highest power setting:

$$Q = VI \tag{F.19}$$

$$\delta Q = \left[\left(\frac{\partial \dot{Q}}{\partial V_1}\delta V_1\right)^2 + \left(\frac{\partial \dot{Q}}{\partial I_1}\delta I_1\right)^2\right]^{\frac{1}{2}} \tag{F.20}$$

$$\delta Q = [(I_1\delta V_1)^2 + (V_1\delta I_1)^2]^{\frac{1}{2}} \tag{F.21}$$

F.5.5   HEAT FLUX

The heat flux uncertainty was calculated by:

$$q = \frac{Q}{A} \tag{F.22}$$

$$\delta q = \left[\left(\frac{\partial q}{\partial Q}\delta Q\right)^2 + \left(\frac{\partial q}{\partial A}\delta A\right)^2\right]^{\frac{1}{2}} \tag{F.23}$$

$$\delta q = \left[\left(\frac{1}{A}\delta Q\right)^2 + \left(\frac{-Q}{A^2}\delta A\right)^2\right]^{\frac{1}{2}} \tag{F.24}$$

F.5.6   SURFACE TEMPERATURE

The surface temperature error also incorporated the EMF error, which was first calculated for the embedded thermocouple temperatures.

The surface temperature uncertainty was calculated by:

$$T_s = T_{embedded} - \left(\frac{\frac{q}{A}L}{k}\right) \tag{F.25}$$

$$\delta T_s = \left[\left(\frac{\partial T_s}{\partial T_{embedded}}\delta T_{embedded}\right)^2 + \left(\frac{\partial T_s}{\partial \frac{q}{A}}\delta \frac{q}{A}\right)^2 + \left(\frac{\partial T_s}{\partial L}\delta L\right)^2 + \left(\frac{\partial T_s}{\partial k}\delta k\right)^2\right]^{\frac{1}{2}} \tag{F.26}$$

$$\delta T_s = \left[(\delta T_{embedded})^2 + \left(\frac{-L}{k}\delta \frac{q}{A}\right)^2 + \left(\frac{-\frac{q}{A}}{k}\delta L\right)^2 + \left(\frac{\frac{q}{A}L}{k^2}\delta k\right)^2\right]^{\frac{1}{2}} \tag{F.27}$$

F.5.7   HEAT TRANSFER COEFFICIENT

The outlet inner-glass fluid temperature was only added during the testing of the third rod, which left the first two rods and a few repetitions of the third rod without any outlet inner-glass fluid

temperature. These temperatures were assumed from averages of the already established tests. A sensitivity analysis was conducted to quantify the error of this assumption by calculating the heat transfer coefficients with the minimum and maximum outlet inner-glass fluid temperatures. This rendered a model which could be implemented in the uncertainty analysis. The worst-case scenario was taken.

The heat transfer coefficient uncertainty was calculated by:

$$h = \frac{q}{(T_s - T_f)} \tag{F.28}$$

$$\delta h = \left[\left(\frac{\partial h}{\partial q} \delta q \right)^2 + \left(\frac{\partial h}{\partial T_s} \delta T_s \right)^2 + \left(\frac{\partial h}{\partial T_f} \delta T_f \right)^2 \right]^{\frac{1}{2}} \tag{F.29}$$

$$\delta h = \left[\left(\frac{1}{(T_s - T_f)} \delta q \right)^2 + \left(\frac{-q}{(T_s - T_f)^2} \delta T_s \right)^2 + \left(\frac{q}{(T_s - T_f)^2} \delta T_f \right)^2 \right]^{\frac{1}{2}} \tag{F.30}$$

F.5.8   NUSSELT NUMBER

The Nusselt number uncertainty was calculated by:

$$Nu = \frac{h D_h}{k} \tag{F.31}$$

$$\delta Nu = \left[\left(\frac{\partial Nu}{\partial h} \delta h \right)^2 + \left(\frac{\partial Nu}{\partial D_h} \delta D_h \right)^2 + \left(\frac{\partial Nu}{\partial k} \delta k \right)^2 \right]^{\frac{1}{2}} \tag{F.32}$$

$$\delta Nu = \left[\left(\frac{D_h}{k} \delta h \right)^2 + \left(\frac{h}{k} \delta D_h \right)^2 + \left(-\frac{h D_h}{k^2} \delta k \right)^2 \right]^{\frac{1}{2}} \tag{F.33}$$

F.5.9   FLOW PRESSURE DROP

The flow pressure drop and dynamic pressure uncertainties were calculated by:

$$\Delta P_{flow} = (P_{in} - P_{out}) - P_{static} \tag{F.34}$$

$$\delta\Delta P_{flow} = \left[\left(\frac{\partial \Delta P_{flow}}{\partial P_{in}}\delta P_{in}\right)^2 + \left(\frac{\partial \Delta P_{flow}}{\partial P_{out}}\delta P_{out}\right)^2 + \left(\frac{\partial P_{flow}}{\partial P_{static}}\delta P_{static}\right)^2\right]^{\frac{1}{2}}$$

(F.35)

$$\delta\Delta P_{flow} = [(\delta P_{in})^2 + (-\delta P_{out})^2 + (-\delta P_{static})^2]^{\frac{1}{2}}$$

(F.36)

F.5.10   VELOCITY

The Reynolds number was averaged between all the rods at 6.4kg/s.

The outlet inner-glass velocity uncertainty was calculated by:

$$V = \sqrt{\frac{2D_h(\Delta P - \rho g \Delta Z)}{\rho f L}}$$

(F.37)

$$V = \frac{1.41 D_h^{\frac{1}{2}}\Delta P^{\frac{1}{2}}}{\rho^{\frac{1}{2}}f^{\frac{1}{2}}L^{\frac{1}{2}}} - \frac{1.41 D_h^{\frac{1}{2}}g^{\frac{1}{2}}\Delta Z^{\frac{1}{2}}}{f^{\frac{1}{2}}L^{\frac{1}{2}}}$$

(F.38)

$$\delta V = \left[\left(\frac{\partial V}{\partial D_h}\delta D_h\right)^2 + \left(\frac{\partial V}{\partial \Delta P}\delta \Delta P\right)^2 + \left(\frac{\partial V}{\partial \rho}\delta \rho\right)^2 + \left(\frac{\partial V}{\partial f}\delta f\right)^2 + \left(\frac{\partial V}{\partial L}\delta L\right)^2 \right.$$
$$\left. + \left(\frac{\partial V}{\partial \Delta Z}\delta \Delta Z\right)^2\right]^{\frac{1}{2}}$$

(F.39)

$$\delta V = \left[\left(\frac{0.5(1.41)D_h^{-\frac{1}{2}}\Delta P^{\frac{1}{2}}}{\rho^{\frac{1}{2}}f^{\frac{1}{2}}L^{\frac{1}{2}}} - \frac{0.5(1.41)D_h^{-\frac{1}{2}}g^{\frac{1}{2}}\Delta Z^{\frac{1}{2}}}{f^{\frac{1}{2}}L^{\frac{1}{2}}} \delta D_h \right)^2 \right.$$

$$+ \left(\frac{0.5(1.41)D_h^{\frac{1}{2}}\Delta P^{-\frac{1}{2}}}{\rho^{\frac{1}{2}}f^{\frac{1}{2}}L^{\frac{1}{2}}} \delta \Delta P \right)^2 + \left(\frac{-0.5(1.41)D_h^{\frac{1}{2}}\Delta P^{\frac{1}{2}}}{\rho^{\frac{3}{2}}f^{\frac{1}{2}}L^{\frac{1}{2}}} \delta \rho \right)^2$$

$$+ \left(\frac{-0.5(1.41)D_h^{\frac{1}{2}}\Delta P^{\frac{1}{2}}}{\rho^{\frac{1}{2}}f^{\frac{3}{2}}L^{\frac{1}{2}}} - \frac{-0.5(1.41)D_h^{\frac{1}{2}}g^{\frac{1}{2}}\Delta Z^{\frac{1}{2}}}{f^{\frac{3}{2}}L^{\frac{1}{2}}} \delta f \right)^2 \tag{F.40}$$

$$+ \left(\frac{-0.5(1.41)D_h^{\frac{1}{2}}\Delta P^{\frac{1}{2}}}{\rho^{\frac{1}{2}}f^{\frac{1}{2}}L^{\frac{3}{2}}} - \frac{-0.5(1.41)D_h^{\frac{1}{2}}g^{\frac{1}{2}}\Delta Z^{\frac{1}{2}}}{f^{\frac{1}{2}}L^{\frac{3}{2}}} \delta L \right)^2$$

$$\left. + \left(\frac{-0.5(1.41)D_h^{\frac{1}{2}}g^{\frac{1}{2}}\Delta Z^{-\frac{1}{2}}}{f^{\frac{1}{2}}L^{\frac{1}{2}}} \delta \Delta Z \right)^2 \right]^{\frac{1}{2}}$$

F.5.11   REYNOLDS NUMBER

The Reynolds number uncertainty was calculated by:

$$Re = \frac{\rho V D_h}{\mu} \tag{F.41}$$

$$\delta Re = \left[\left(\frac{\partial Re}{\partial \rho} \delta \rho \right)^2 + \left(\frac{\partial Re}{\partial V} \delta V \right)^2 + \left(\frac{\partial Re}{\partial D_h} \delta D_h \right)^2 + \left(\frac{\partial Re}{\partial \mu} \delta \mu \right)^2 \right]^{\frac{1}{2}} \tag{F.42}$$

$$\delta Re = \left[\left(\frac{V D_h}{\mu} \delta \rho \right)^2 + \left(\frac{\rho D_h}{\mu} \delta V \right)^2 + \left(\frac{\rho V}{\mu} \delta D_h \right)^2 + \left(\frac{-\rho V D_h}{\mu^2} \delta \mu \right)^2 \right]^{\frac{1}{2}} \tag{F.43}$$

F.5.12   FRICTION FACTOR

The Haaland equation was used with a maximum error of 2%. This error was used when analysing the pump head uncertainty.

F.5.13   COLBURN J-FACTOR

The Colburn J-factor uncertainty was calculated by:

$$j = \frac{Nu}{RePr^{\frac{1}{3}}} \tag{F.44}$$

$$\delta j = \left[\left(\frac{\partial j}{\partial Nu} \delta Nu \right)^2 + \left(\frac{\partial j}{\partial Re} \delta Re \right)^2 + \left(\frac{\partial j}{\partial Pr} \delta Pr \right)^2 \right]^{\frac{1}{2}} \tag{F.45}$$

$$\delta j = \left[\left(\frac{1}{RePr^{\frac{1}{3}}} \delta Nu \right)^2 + \left(\frac{-Nu}{Re^2 Pr^{\frac{1}{3}}} \delta Re \right)^2 + \left(\frac{(-\frac{1}{3})Nu}{RePr^{\frac{4}{3}}} \delta Pr \right)^2 \right]^{\frac{1}{2}} \tag{F.46}$$

F.6 RESULTS

The final uncertainties can be found in **Tables F.3**. The heat transfer area error used in the final uncertainty results was:

$$\delta A = 4.5352E - 5\ m^2, (0.31\%\ Error)$$

The flow pressure drop error used in the final uncertainty results was:

$$\Delta P_{flow} = 2598.08 Pa, (1.73\%\ Error)$$

Table F: Calculation uncertainties

	Maximum uncertainty (%)
Heat flux, $\frac{q}{A}$	10.67
Heat transfer coefficient, h	8.07
Nusselt Number, Nu	8.23
Velocity, V	30.15
Reynolds number, Re	19.60
Colburn J-Factor, j	21.12

F.7 SUMMARY

The purpose of an uncertainty analysis is to quantify the error that the measurement process inherently has by breaking down each component.

The linear regression analysis was used for the thermocouples, heat input and the EMF effect uncertainties, while most of the equipment uncertainties were taken to be bias uncertainties provided by the supplier. The precision data was gathered from the results.

The final uncertainties faired reasonably well with the biggest uncertainty being the velocity. This was to be expected but with all considerations taken into account this final value is good due to the physical constraints of the test piece.